Coupling on a multilayer printed circuit board and the current distribution in the ground plane

Eindhoven University of Technology Research Reports

EINDHOVEN UNIVERSITY OF TECHNOLOGY

Faculty of Electrical Engineering
Eindhoven, The Netherlands

ISSN 0167-9708 Coden: TEUEDE

COUPLING ON A MULTILAYER PRINTED CIRCUIT BOARD AND THE CURRENT DISTRIBUTION IN THE GROUND PLANE

by

F. B. M. van Horck
A. P. J. van Deursen
P. C. T. van der Laan

EUT Report 96-E-300
ISBN 90-6144-300-8

Eindhoven
May 1996

CIP-DATA LIBRARY TECHNISCHE UNIVERSITEIT EINDHOVEN

Horck, F.B.M. van

Coupling on a multilayer printed circuit board and the current distribution in the ground plane / by F.B.M. van Horck, A.P.J. van Deursen and P.C.T. van der Laan. - Eindhoven : Eindhoven University of Technology, 1996. - VI, 47 p. - (Eindhoven University of Technology research reports ; 96-E-300).
ISBN 90-6144-300-8
NUGI 832
Trefw.: elektromagnetische interferentie / gedrukte bedrading / elektromagnetische koppelingen.
Subject headings: electromagnetic compatibility / multilayer boards / crosstalk.

Coupling on a Multilayer Printed Circuit Board and the Current Distribution in the Ground Plane

F. B. M. van Horck, A. P. J. van Deursen and P. C. T. van der Laan

Abstract

The current distribution in the ground plane (GP) has been studied for a triple layer printed circuit board (PCB). The continuous GP was the middle layer; test tracks were placed at various positions in the top and bottom layer. The crosstalk or transfer impedance Z_t between tracks on opposite sides of the GP is particularly sensitive to the current distribution in the GP. Common mode current distributions and the crosstalk or Z_t to circuits on the PCB were studied as well. The 2D-calculations rely on different models, each valid for a specific frequency range. General analytical expessions for Z_t are given. Measurements between 10 Hz and 1 GHz confirm the models. Practical applications using the results as 'design rules' are discussed.

Keywords: electromagnetic compatibility, EMC, electromagnetic interference, EMI, multilayer boards, crosstalk, transfer impedance, printed circuit board, PCB printed wiring board, PWB, common mode currents, design rules, layout printed circuit.

Horck, F. B. M. van and A. P. J. van Deursen, P. C. T. van der Laan
Coupling on a multilayer printed circuit board and the current distribution in the ground plane.
Eindhoven: Faculty of Electrical Engineering, Eindhoven University of Technology, 1996.
EUT Report 96-E-300, ISBN 90-6144-300-8

Address of the authors:
High Voltage and EMC Group
Faculty of Electrical Engineering
Eindhoven University of Technology
P.O. Box 513, 5600 MB Eindhoven, The Netherlands

E-mail: f.b.m.v.horck@ele.tue.nl
a.p.j.v.deursen@ele.tue.nl
p.c.t.v.d.laan@ele.tue.nl

Acknowledgement

This research is supported by the Dutch Technology Foundation (STW) in project number ETN11.2508. The skillful support by P.R. Bruins in many of the measurements is gratefully acknowledged.

Contents

Coupling on a Multilayer Printed Circuit Board and the Current Distribution in the Ground Plane

I. Introduction

In multilayer printed circuit boards (PCB), ground connections are often made to continuous metallic planes which extend over the full PCB. A ground plane (GP) serves several purposes simultaneously. First the GP provides a return path for the signal current through the tracks. Secondly, the GP forms a path for a common mode (CM) current which may arrive at the PCB via cables connected to the PCB [1]. Thirdly, an external perpendicular magnetic field may induce a pattern of circulating currents in the GP. The current distribution over the plane is important for crosstalk between different signal circuits on the PCB, for sensitivity with respect to external disturbances, and for generation of such disturbances [2]. The many tracks on a PCB often follow complicated paths. The EMC behavior is then difficult to analyze. Most computer programs for signal transport and EMC parameters translate the electromagnetic (EM) fields by parameters for transmission line and circuit theory, and then solve the resulting equations. The EM fields become hidden in this process. However, design rules can be obtained from the current distribution and the associated magnetic field, even for simple geometries of a PCB.

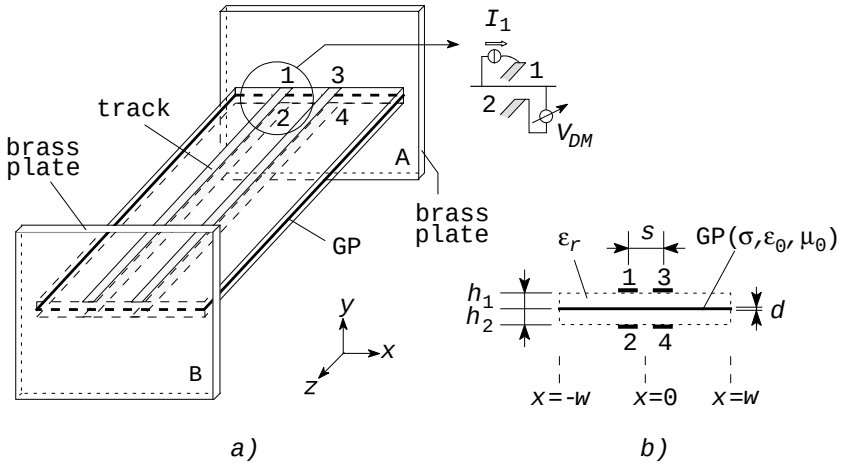

Fig. 1. a) Four tracks on a triple layer PCB which is mounted between two brass plates A and B. The tracks and the ground plane are shorted to plate B. The current injected in track 1 on top returns through the ground plane (middle layer); the voltage is measured between track 2 (lowest layer) and the ground plane. b) cross-section of the PCB.

We carried out a two-dimensional theoretical study of a model PCB which had a single GP and parallel tracks. Our experimental triple layer PCB was also analyzed in terms of a

2D-geometry. The GP was the middle layer; tracks were placed at various positions relative to each other and to the edges of the PCB (Fig. 1). The tracks, the electronic components at their ends, and the GP form closed signal loops or differential mode (DM) circuits. We are mainly interested in spurious couplings, although the signal transport proper can be analyzed by a similar approach. We replaced all electronics at one end of the tracks by a short circuit to the GP. At the other end we connected one track to a voltmeter which measured the effect of a current injected in another track (DM to DM crosstalk) or injected elsewhere in the GP (CM to DM crosstalk). The ratio of voltage to current can be represented by a transfer impedance Z_t. This Z_t is related to the current distribution in the GP and the associated magnetic field which both depend on frequency in a complicated way. The CM current is injected through a second plate, e.g. a cabinet panel at some distance under the PCB. We use the acronym CP for the cabinet panel. Because of reciprocity, the Z_t between the CM and the DM circuits also governs the CM current generation by the DM circuits on the PCB. For both DM-DM and DM-CM crosstalk the coupling through the electric field, or the transfer admittance Y_t, is not discussed here.

Numerous papers deal with the DM to DM crosstalk between tracks on the same side of a GP, e.g. tracks 1 and 3 in Fig. 1. Gravelle and Wilson [3] give an extended list of references. Often the high frequency (HF) limit is used, valid above about 30 MHz for a copper GP of 30 μm thickness; above this frequency the current distribution in the GP does not change anymore. The HF limit is certainly a good approach when modern high speed digital electronics is considered. However, there are many important low frequency applications such as transducers and amplifiers for slow signals like temperature, level and position, and electronics for audio and video. Most switched-mode power supplies operate at frequencies below 1 MHz. At lower frequencies the resistivity of the GP alters the current distribution [4].

Both inductive and capacitive coupling are reduced when we place the tracks at opposite sides of the GP. The DM to DM crosstalk is then more sensitive to the current distribution in the GP. Actually we employed this type of crosstalk to study the current distribution in the GP [5, 6].

The calculations are based on 2D potential theory where we emphasize the coupling by the magnetic field. The tracks were replaced by filamentary wires. We derived general analytical approximations for the Z_t or the relevant parts thereof, or we present expressions for track positions which can be regarded as extreme cases. Such guidelines can help a designer to estimate beforehand the EMC properties of signal circuits. Some integral equations had to be solved numerically. The spurious couplings require considerable accuracy in the calculations; therefore the analytical and numerical results are compared in order to check consistency and accuracy. In order to retain clarity of the paper, all mathematical details are deferred to Annexes. In Sect. II we discuss a physical picture for the current distribution and the DM-DM crosstalk which provides a simple way to understand the results for an isolated PCB. Section III describes the calculations and additional results. The Z_t for the CM to DM coupling is discussed in Sect. IV. The proximity of a metal cabinet panel influences the magnetic field and alters the DM to DM crosstalk; in Section V we present a choice out of the many possible configurations. A signal track between two ground planes and its coupling to another DM circuit outside these planes is studied in Section VI. Section VII presents the measurements and compares them with the theory. Some practical examples are given in Sect. VIII.

The experimental triple layer PCB was 20 cm long. The copper GP had a conductivity

$\sigma = 5.8 \cdot 10^7 (\Omega\text{m})^{-1}$ and a thickness $d = 30$ μm. The width $2w$ of the GP was often 50 mm, although wider GP's were used as well. The 1.5 mm wide tracks were placed at $h_{1,2} = 1.5$ mm above and below the GP (see Fig. 1). The epoxy layer on both sides of the GP had a dielectric constant ε_r of 4.7. Two large brass plates mounted perpendicularly at the ends of the PCB formed a mirror for the magnetic field, thus simulating a 2D-geometry. The GP was connected over the full width to the brass plates; the CP only at one end to allow CM current injection. Measurements are carried out at frequencies between 10 Hz and 1 GHz. The DM-DM Z_t's show a variety of phenomena below 100 MHz. Resonances in Z_t due to the finite length of the PCB show up at higher frequencies. In addition, the surroundings of the PCB may affect the resonances in frequency and in amplitude. Calculations including these 3D-effects are not reported here.

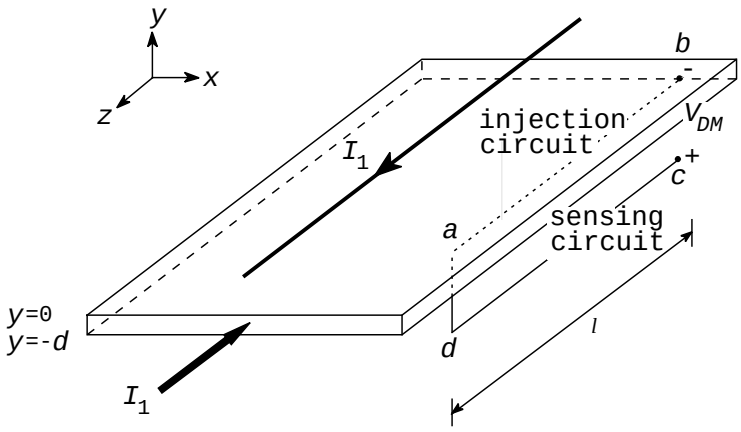

Fig. 2. The voltage V_{DM} measured between c and b is determined by the E_z-field along the line a-b and the flux through the area a-b-c-d-a.

II. General behavior of the current distribution and the Z_t between tracks

For a physical picture of the phenomena governing the transfer impedance Z_t, we consider the $Z_t(1,2)$ between tracks 1 and 2, for the moment centered ($x_{1,2} = 0$) on the GP ($2w = 5$ cm) at opposite sides. The origin of the coordinate system is placed at the center of the upper surface of the GP. The current I_1 is injected in track 1 and returns via the short circuit and the GP. The DM voltage V_{DM} between track 2 and the GP is determined at the sending end for the current. Faraday's law for time harmonic signals $\oint \mathbf{E} \cdot d\mathbf{l} = -j\omega\Phi$ yields

$$\begin{aligned} V_{DM} &= \int_a^b E_z(x,-d)\, dl + j\omega\Phi \\ &= E_z(x,-d)\ell + j\omega\Phi \\ &= Z_t I_1 \ell, \end{aligned} \tag{1}$$

where Φ is the flux through the rectangle a-b-c-d-a in Fig. 2. The electric field $E_z(x,-d)$ at the lower surface of the GP is related to the local current density by $J_z(x,-d)/\sigma$. The 2D

assumption allows the second and third line in Eq. (1); here Z_t is the transfer impedance per unit length.

The solid line in Fig. 3a shows the general behavior of $Z_t(1,2)$ for a thin GP without skin effect; Fig. 3b shows the absolute values of the contribution to Z_t as calculated in Sect. IIIb: a) $E_z(0,-d)$, and the flux between the GP and track 2 as b) $j\omega\Phi_1$ due to the vacuum magnetic field of track 1, and c) $j\omega\Phi_{GP}$ due to the current density in the GP. At low frequencies the variation of $J_z(x,y)$ with depth y in the GP may be neglected. We can write the volume current density J_z as a sheet current density K_z

$$K_z(x) = \int_{-d}^{0} J_z(x,y)dy, \tag{2}$$

or simpler here: $K_z(x) = dJ_z(x,y)$. The E_z is related to K_z through $E_z(x,-d) = R_\square K_z(x)$, where $R_\square = 1/\sigma d$ is the sheet resistance of the GP.

Below 1 kHz (region 1 in Fig. 3a) the current density K_z is also homogeneous in the x-direction. The Z_t is given by the d.c. resistance of the GP, $Z_t(\omega = 0) = R_\square/2w$ or 11.5 mΩ/m for our PCB. The vacuum magnetic field due to the current in track 1 and the current in the GP fully penetrates the GP (Fig. 4a). However, the flux contributions to Z_t are still negligible. Above 1 kHz the J_z concentrates under the track (Fig. 4b) in order to expel the magnetic field out of the GP. The E_z contribution to $Z_t(1,2)$ increases. At 300 kHz (region 3) the current distribution in the GP becomes nearly independent of frequency in the vicinity of track 1. Its value tends to

$$K_z(x) = -\frac{I_1}{\pi}\frac{h_1}{x^2 + h_1^2}, \tag{3}$$

analogous to the electrostatic surface charge distribution induced on the GP when a wire with charge q per unit length is above that plane, see any introductory text book on electromagnetics, e.g. Ramo *et al.* [7]. The E_z remains related to the K_z. The change in E_z between region 1 and 3 is a factor $2w/\pi h_1$, i.e. a factor 10.6 for our PCB (see Fig. 3b). The flux contributions lower the change in Z_t. The total Z_t is constant over nearly two decades in frequency. Both flux contributions $j\omega\Phi_1$ and $j\omega\Phi_{GP}$ become similar in magnitude but opposite in phase. The calculations in Sect. III show that the total flux $\Phi_1 + \Phi_{GP}$ decreases with $1/\omega$, which results in the constant Z_t of Eq. (13).

An analogous situation occurs in the more familiar magnetic shielding of a long tube [8] for an external homogeneous axial magnetic field (Fig. 5). An external field H_e produces a flux through the tube $\Phi_e = \mu_0 H_e \pi r_t^2$. In the tube wall a circulating current I_t produces a flux $L_t I_t$ through the tube. Here $L_t = \mu_0 \pi r_t^2/\ell_t$ is the self inductance of the tube regarded as a long single turn coil of length ℓ_t. The resistance of the tube for the circulating current is $R_t = 2\pi r_t/d_t\ell_t\sigma_t$, with d_t the wall thickness and σ_t the conductivity. We again assume here that the current is homogeneous over the wall thickness. Faraday's law then results in

$$R_t I_t = -j\omega\Phi_e - j\omega L_t I_t. \tag{4}$$

At low frequencies, $\omega \ll R_t/L_t$ the total flux inside the tube $\Phi_e + L_t I_t \approx \Phi_e$ because the current I_t is low. At high frequencies the flux tends to zero as $\Phi_e R_t/(R_t + j\omega L_t)$. A voltage induced in a loop inside the tube becomes independent of frequency in this model. The cross-over frequency is given by $\omega L_t = R_t$ or $r_t d_t = \delta^2$. Here $\delta = \sqrt{2/\omega\mu_0\sigma_t}$ is the skin depth for the tube with $\mu_r = 1$ because the flux inside the tube is involved rather than the flux in the tube wall. The relation $r_t d_t = \delta^2$ also holds for the onset of shielding against a magnetic field

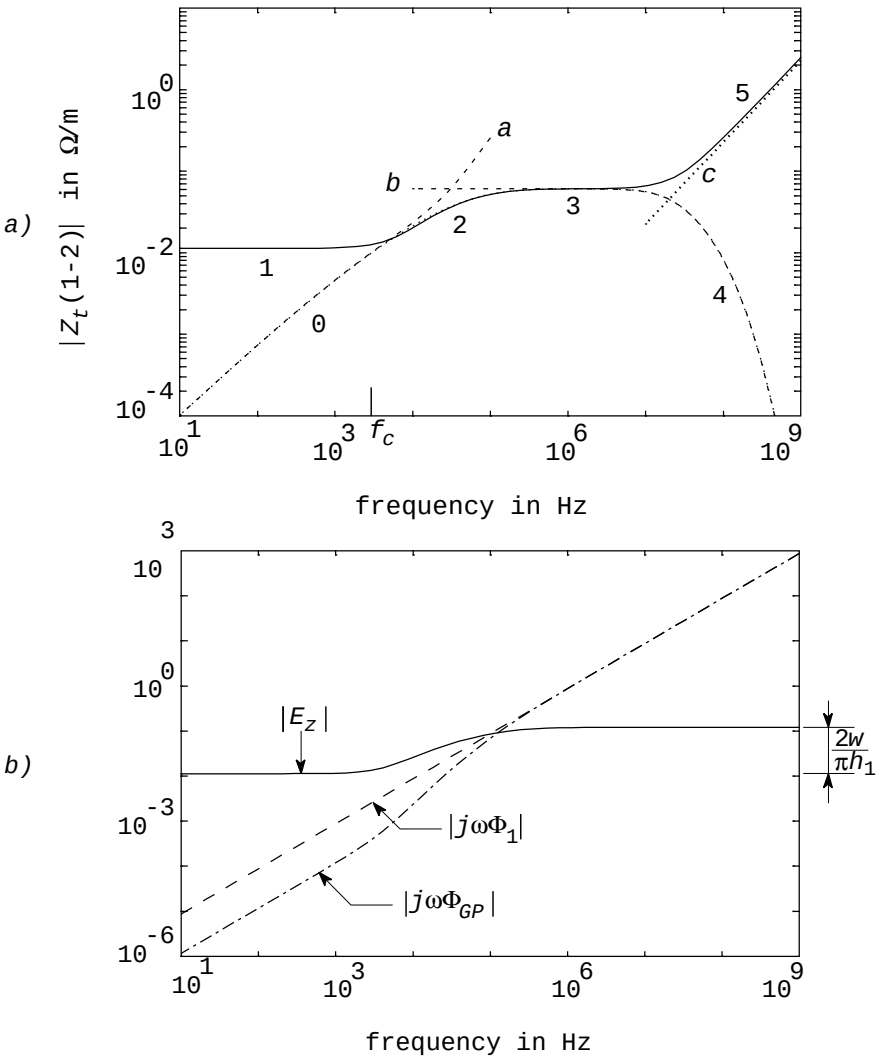

Fig. 3. a) General behavior of $|Z_t(1\text{-}2)|$ between track 1 and 2 with a $2w = 5$ cm wide GP. The curve 1-2-3-5 (—) is calculated by method of moments (Sect. IIIb). The curve 0-2-3-4 ($- \cdot - \cdot -$) shows $|Z_t(1\text{-}2)|$ for a very wide ground plane; the skin effect then lowers the $|Z_t(1\text{-}2)|$ in region 4. The asymptotes a, b and c are discussed in the text, Sect. III, as is $f_c = 2.9$ kHz from Eq. (5). b) Contributions to $|Z_t(1\text{-}2)|$ from Eq.(1); Φ_1 and Φ_{GP} represent the flux between track 2 and the GP due to the vacuum field of track 1 and of the GP, respectively.

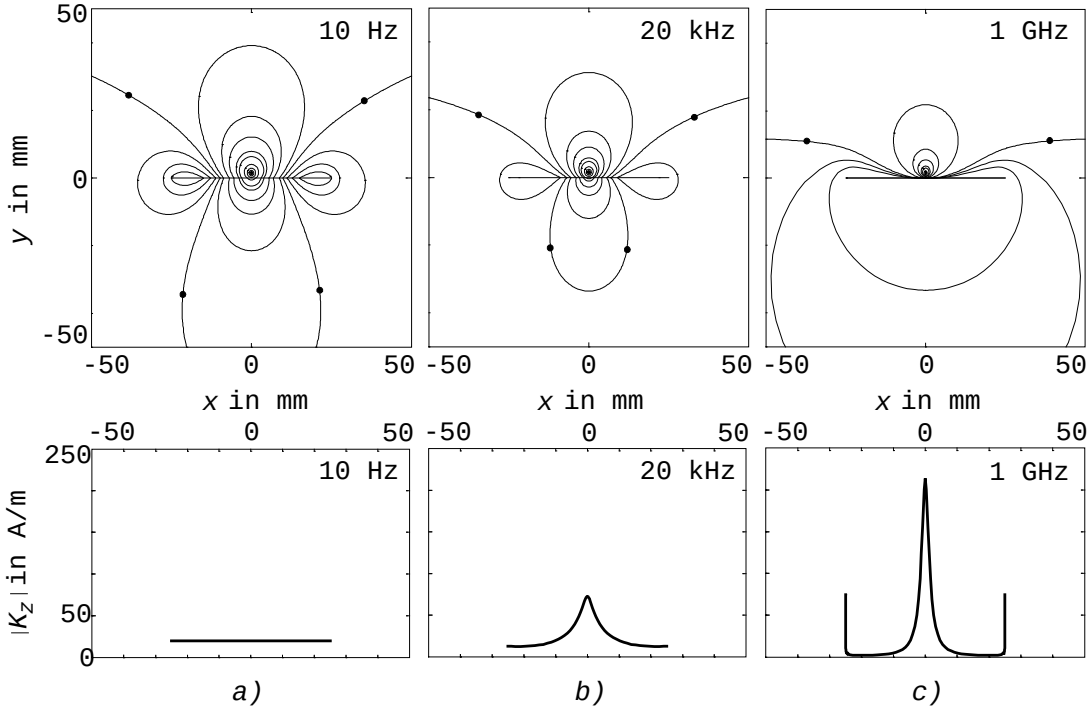

Fig. 4. Magnetic field lines and current distribution $|K_z|$ in the ground plane ($2w = 5$ cm) for three frequencies. Only at large distance of the GP the field lines assume the dipolar shape, i.e. closed circles through the dipole. The marked field lines are the separatrices $A_z = 0$ between the field lines, which at large distance close above or under the GP.

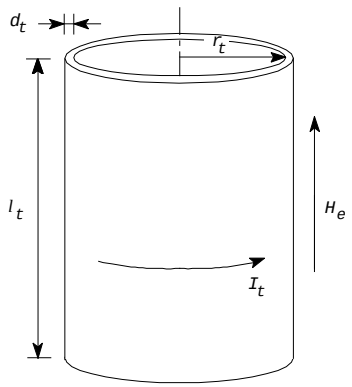

Fig. 5. Parameters for the tube analogon.

perpendicular to the tube axis [9, p. 81]. Returning to our PCB we extend this analogy and estimate the cross-over frequency f_c between region 1 and 2 by the relation $2wd = \delta^2$:

$$f_c = R_\square / 2\pi\mu_0 w \tag{5}$$

valid for the mid position $x \approx 0$ of both tracks. A more accurate estimate requires the solution of the implicit equation $R_\square = |Z_t|$ with Z_t given by Eq. (12) in Sect. IIIa.

Above 10 MHz two effects become discernible. First the current density approaches the HF limit under track 1 given by Eq. (3). The magnetic field through the GP is strongly reduced. For an infinitely wide GP, the two flux contributions Φ_1 and Φ_{GP} would become equal and opposite. However, because of the finite width some magnetic field lines wrap around the GP (Fig. 4c). The flux between track 2 and the GP is then given by the residual difference of the flux contributions which can be described by a frequency independent mutual inductance M (region 5 and asymptote c in Fig. 3a). From Kaden [9, p. 266] or Love [10, Sect. 13] one has

$$M = \frac{\mu_0}{4\pi}\frac{h_1 h_2}{w^2}, \tag{6}$$

valid near $x = 0$ for both tracks. At the edges of the GP $K_z(x)$ approaches the HF limit near $|x| = w$:

$$K_z(x) \propto 1/\sqrt{w^2 - x^2}, \tag{7}$$

analogous to the edge effect for charge density on a plate. The magnetic field near the edges is strong. However, the current density diverges only in thin strips near the edges of the GP. Because of the small area involved, the flux through these strips is small. Only at high frequencies the resistance will then be overruled by induction, in our example at frequencies larger than 30 MHz; the GP then behaves like an ideal conductor ($\sigma \to \infty$).

Secondly, the skin effect alters the vertical current distribution in the GP. For an infinitely wide GP with permeability $\mu = \mu_r\mu_0$ the high frequency Z_t is given by:

$$Z_t = R_\square \frac{kd}{\sinh kd}\frac{h_t}{\pi(x^2 + h_t^2)}, \tag{8}$$

in which $h_t = h_1 + h_2$ and $k = (1+j)/\delta$ with $\delta = \sqrt{2/\omega\mu_0\mu_r\sigma}$ the skin depth. This behavior is shown by the dot-dash line, region 3 and 4 in Fig. 3a, and by the asymptote b. For the 50 mm wide GP of our example, the exponential decrease in Z_t by the skin effect is overruled by the increase due to the flux coupling around the GP. The transfer impedance of a thin walled tube [9, 11], considered as outer conductor of a coaxial system, decreases in an analogous fashion:

$$Z_t = R_0 \frac{kd_t}{\sinh kd_t}, \tag{9}$$

where R_0 is approximately the d.c. resistance of the tube per meter, and d_t the wall thickness of the tube. The current flows in the longitudinal direction through the tube wall; the current distribution is axially symmetric. The additional x-dependence in Eq. (8) stems from the distribution of the current over the GP. A similar exponential decrease also sets in at $d_t \approx \delta$ for the shielding of the tube mentioned above [9, pp. 292-295]. Some authors call the current contraction under track 1 the lateral skin effect or just skin effect [12]. In this paper the vertical skin effect is meant when the term vertical is omitted.

Note that the perpendicular component $H_\perp$ of the magnetic field at the surface of the GP never vanishes exactly for a GP with finite conductivity. The y-component of $\nabla \times \mathbf{E} = -j\omega\mathbf{B}$

links the x-variation of the current density σE_z to the $H_\perp$. In region 3 (Fig. 3a) the magnetic field penetrates the GP and leaves at the other side of the GP; in region 4 the magnetic field $H_\perp$ at the surface is guided through the skin. The penetration is more pronounced where the variation of the current density is larger, i.e. near the edges and under track 1 as discussed before.

III. Mathematical description

a. The half space and the infinite plate

In a first step consider the plane $y = 0$ limiting the lower half space (Fig. 6a) of material with conductivity σ and magnetic permeability $\mu = \mu_0\mu_r$. The filamentary wire carrying the injection current I_1 is in the dielectric region (ε_0, μ_0) at a height h_1 above the plane. The distribution of the induced return current $J_z(x, y)$ in the plane has already been calculated by Carson [13] in 1926 for non-magnetic materials ($\mu_r = 1$). He assumed a transverse magnetic wave $\propto e^{j\omega t-\gamma z}$ propagating in the positive z-direction with a small propagation constant γ.

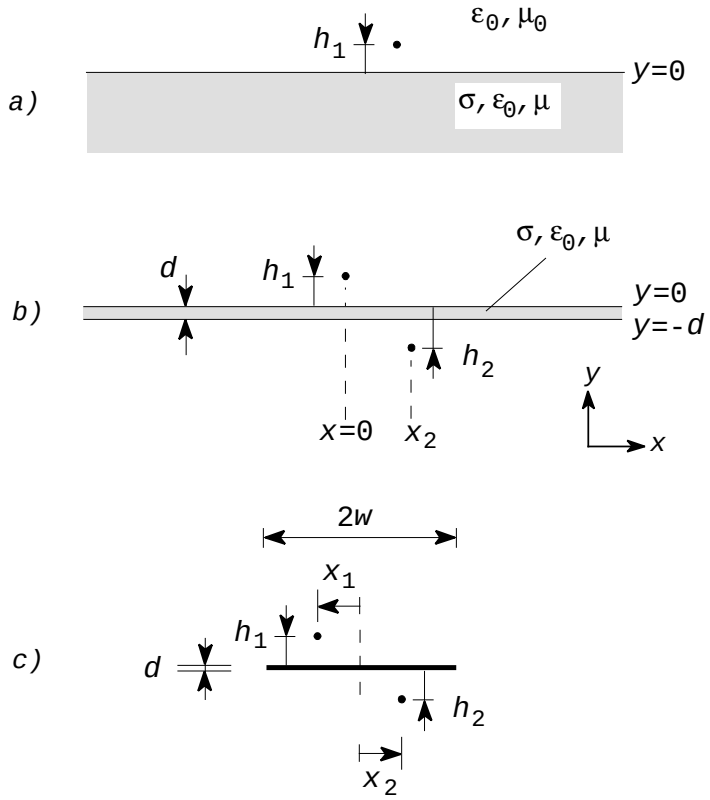

Fig. 6. Parameters for a) the infinite plane, b) the infinite plate, and c) the strip or finite plate.

Carson aimed at a telegraph wire several meters above soil with typical conductivity of about 10^{-2} $(\Omega\mathrm{m})^{-1}$. Many authors [14, 15, 16, 17] treated the transmission of waves along wires above a dissipative medium; some use the full wave analysis. For our PCB Carson's approach is apparently correct up to the GHz range because of the much smaller distances

between tracks and GP and the high conductivity of copper. Appendix A1 gives the general steps of Carson's derivation, which is slightly extended in order to incorporate magnetic materials $\mu_r \neq 1$; see also [18].

In a second step consider the plate at $y = 0$ with thickness d and conductivity σ, still of infinite extent in the x-direction (Fig. 6b). The injection wire is at the position $(0, h_1)$ above the upper side of the plate; a sensing wire is at $(x_2, -h_2)$ below the plate. In both dielectric regions $\mu_r = 1$ is assumed. Since we do only consider the coupling by the Z_t, we may also take $\varepsilon_r = 1$. Because of the finite conductivity, the magnetic field penetrates the plate. An inductive coupling exists between the circuits at both sides of the GP. In Appendix A2, Carson's calculation for the longitudinal current distribution $J_z(x, y)$ in the plate is extended to allow a finite thickness d of the plate (Eq. (A13)) and to include the magnetic field below the plate.

For a thin GP one may take the 'thin plate limit' $d \downarrow 0$ and $\sigma \to \infty$ while keeping the sheet resistance $R_\square$ of the plate constant. The sheet current density K_z can be derived from the current density $J_z(x, y)$ in Eq. (A13):

$$K_z(x) = \int_{-d}^{0} J_z(x, y)\,\mathrm{d}y = -\frac{j\omega\mu_0 I_1}{2\pi R_\square} \int_0^\infty \frac{\cos(\alpha x)\,\mathrm{e}^{-\alpha h_1}}{\alpha + j\beta}\,\mathrm{d}\alpha, \tag{10}$$

in which $\beta = \omega\mu_0/2R_\square$. Asymptotic expressions for Z_t can also be derived in closed form. After some algebra using Eq. (A17), the transfer impedance for the sensing wire at $(x_2, -h_2)$ under the GP simplifies to

$$Z_t = \frac{j\omega\mu_0}{2\pi} \int_0^\infty \frac{\cos(\alpha x_2)\mathrm{e}^{-\alpha h_t}}{\alpha + j\beta}\,\mathrm{d}\alpha, \tag{11}$$

in which $h_t = h_1 + h_2$. For low frequencies the small argument expansion [19] of the Ei functions in Eq. (A18) yields

$$Z_t = \frac{1}{4}\omega\mu_0 - j\frac{\omega\mu_0}{2\pi}\left[\ln\frac{\omega\mu_0(x_2^2 + h_t^2)^{\frac{1}{2}}}{2R_\square} + \gamma\right], \tag{12}$$

with $\gamma = 0.57721\cdots$ Euler's constant. This Z_t is the asymptote labeled a in Fig. 3a. The high frequency approximation of Eq. (11) reduces to

$$Z_t = R_\square \frac{h_t}{\pi(x_2^2 + h_t^2)}. \tag{13}$$

This Z_t value (region 3 and asymptote b in Fig. 3a) does not explicitly depend on the frequency. In Eq. (11) only the sum h_t of the heights h_1 and h_2 occurs. Reciprocity only requires that the Z_t is symmetrical in h_1 and h_2. Remarkably the position of the thin GP between the track does not influence this part of Z_t.

In the thin plate limit no skin effect is possible since d/δ goes to zero. In order to correctly describe the skin effect we must consider a general thickness d and use the full equation (A17). The resulting Z_t is displayed as curve 0-2-3-4 in Fig. 3a. Fortunately the expression simplifies in the high frequency limit to Eq. (8). The frequency f_{cs} where the skin effect becomes effective, can be calculated explicitly. Choose, by convention, the 3 dB point where $|Z_t|^2$

obtained by Eq. (8) is halved with regard to the value of region 3 in Fig. 2 given by Eq. (13). The transcendental equation

$$\left|\sinh\left[(1+j)\frac{d}{\delta}\right]\right| = 2\frac{d}{\delta}, \tag{14}$$

has an approximate solution $d/\delta \approx 2.14$. Thus the cutoff frequency f_{cs} is given by

$$f_{cs} \approx \frac{2.25}{\pi\mu_0\sigma d^2}, \tag{15}$$

and is again independent of the heights h_1 and h_2. This frequency equals approx. 22 MHz for the GP parameters used in calculating Z_t in Fig. 3a. In Fig. 3a the curve 0-2-3-4 shows the behavior of Z_t as described in this Section. Good agreement is shown in region 2 and 3 (Fig. 3a) between the analytical expressions and the method of moments (MOM) calculations [20] described in the next subsection. The deviations at the low and the high frequency end (region 1 and 5 in Fig. 3a) are due to the finite width of the GP.

b. The strip of finite width

We now replace the infinite plate GP by a strip of width $2w$ (Fig. 6c). The injection current I_1 flows through the wire at the upper side of the strip and returns via the strip. We again consider the thin plate limit and calculate the sheet current density $K_z(x)$. The width $2w$ is less than the shortest wavelength under consideration. We use Faraday's law for two positions $(x, 0)$ and $(x^*, 0)$ on the strip:

$$E_z(x,0) - E_z(x^*,0) = -j\omega\left\{A_z(x,0) - A_z(x^*,0)\right\} \tag{16}$$

in which the vector potential A_z is due to the current I_1 through the injection wire and to the current $K_z = E_z/R_\square$ distributed over the strip, see Appendix B. Here we require that I_1 returns through the strip, or

$$\int_{-w}^{w} K_z(x)\,dx = -I_1, \tag{17}$$

Equation (16) was solved by the method of moments [20]. Step functions as basis functions approximated $K_z(x)$ over intervals of the strip. Point-matching (Dirac delta functions as testing functions) was used. The collocation points were at the middle of subsequent intervals. The vector potential contribution due to each interval was calculated analytically [21]. In order to improve the accuracy with reduced calculation effort, the discretization of the strip was non-uniform: a $(x^2+h_1^2)^{-1}$ partition beneath the injection wire and a fine constant mesh at the edges. The transfer impedance Z_t is then obtained by Eq. (1). The solid line in Fig. 3a is obtained by this MOM method. The total number N of intervals was chosen in such a way that the difference between the analytical HF value of Z_t (see next section) and the numerical one was less than 10 percent. This required an accuracy in the A_z of about 10^{-4}; compare also Fig. 3b. Such accuracy is generally needed in EMC calculations because one looks for spurious couplings close to the currents. No attempts were made to obtain the 'ideal mesh' through rigorous error analysis.

For low frequencies the resistive contribution (E_z term in Eq. (1)) dominates the magnetic flux term, and Z_t is constant. The cross-over frequency f_c between region 1 and 2 was discussed in Sect. II; an approximate expression based on the tube analogon is given in

Eq. (5). The flat region 3 agrees with the analytical expression Eq. (13) for Z_t presented before. At high frequencies the vector potential dominates the resistive term; the l.h.s. of Eq. (16) can be neglected. As a result of the finite width, the transfer impedance in Fig. 3 increases linearly with frequency for $f > 30$ MHz.

When both tracks are close to the edge, the current density concentrates more slowly under track 1; the calculated Z_t is shown in Fig. 7. At high frequency the MOM Z_t is in agreement with the analytical expression Eq. (20) discussed below.

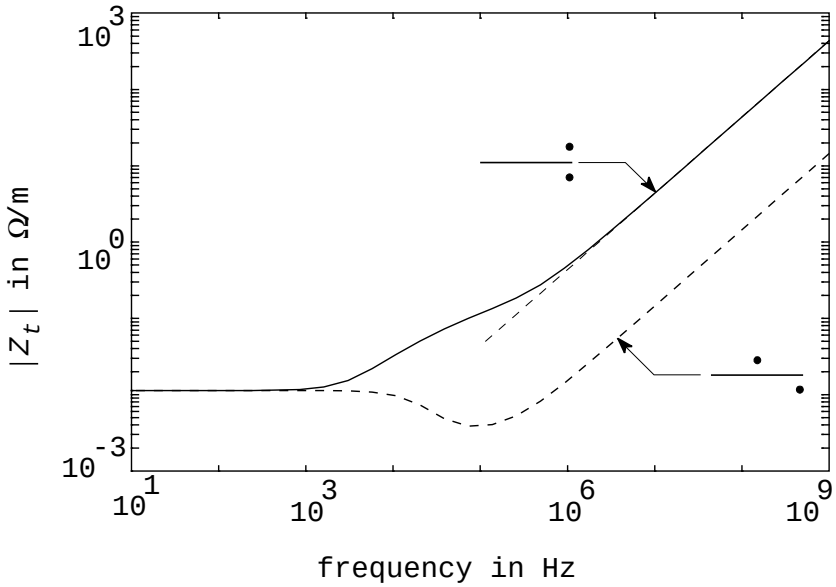

Fig. 7. DM to DM Z_t calculated by MOM for one or both wires at the edge of a 50 mm wide GP. The vertical distance between wires and GP is 1.5 mm. The straight line behavior above 10 MHz corresponds to M-values of Fig. 8.

c. Mutual inductance

For high frequencies the GP can be considered as an thin ($d \downarrow 0$) ideal conductor ($\sigma \to \infty$) with a sheet current distribution K_z. The magnetic field does not penetrate the GP anymore. The magnetic field outside the GP can then be derived from a complex potential Ω which can be obtained by means of conformal transformation. See for details Appendix C1. The current distribution on both surfaces of the strip results from [9, pp. 56-58]

$$K_z(x) = -|\hat{\mathbf{y}} \times \mathbf{H}| = -\mathrm{Re}\frac{d\Omega^*}{dz}, \tag{18}$$

where Ω^* is the conjugated of the complex potential Ω. For an arbitrary position of the injection wire, the result of Eq. (18) is given by Love [10]. For small height-to-width-ratio h_1/w and the injection wire near $x = 0$, his solution [10, Sect. 13] can be approximated by

$$K_z(x) \approx -\frac{I_1}{\pi}\left[\frac{h_1}{x^2 + h_1^2} + \frac{h_1}{w\sqrt{w^2 - x^2}}\right], \tag{19}$$

in which the contribution of Ω at the upper and lower surface are added (see Fig. C1). The first term of the right hand side is the same as the HF distribution for an infinitely thin plate; compare with Eq. (3). The last term results from the edge effect.

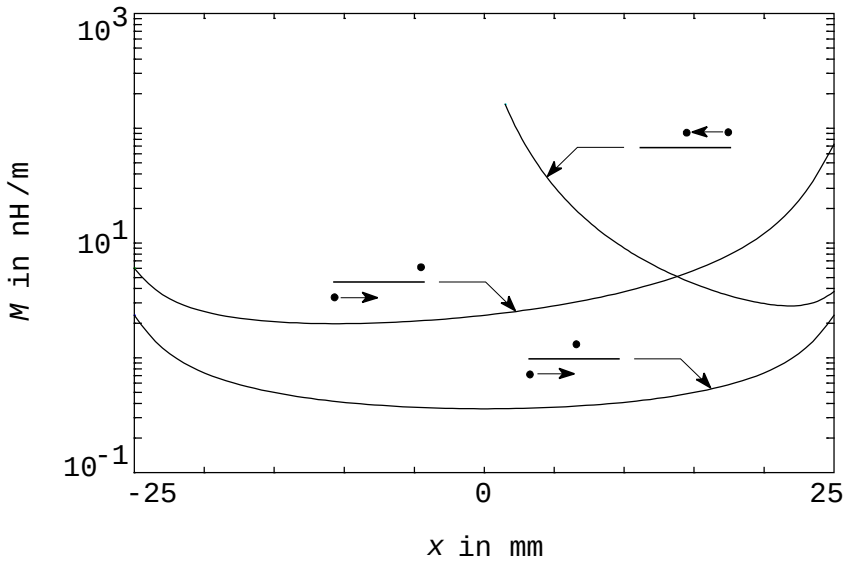

Fig. 8. The mutual inductance part M of Z_t between two DM circuits when one of the circuits moves over the GP along the x-direction. Both tracks are at 1.5 mm distance from the 50 mm wide GP.

The transfer impedance now becomes a frequency independent mutual inductance M which can be calculated by means of Eqs. (C1), (C3), (C4), and (C5) for any position of the two wires. When $h_{1,2} \ll w$ simple real forms exist. The lowest M is given by Eq. (6) for both wires at $x = 0$ on opposite sides of the GP. An upper bound occurs when both wires are at the same edge, $|x| = w$, but still on opposite sides of the GP. For general h_1 and h_2:

$$M(|x| = w) \approx \frac{\mu_0}{4\pi} \ln\left[1 + \frac{2\sqrt{h_1 h_2}}{(h_1 + h_2)}\right], \tag{20}$$

which attains a maximum value when $h_1 = h_2$: $M_2 = (\mu_0/4\pi)\ln 2$. Figure 8 shows a set of M-curves for a GP of $2w = 5$cm and both wires at the same distance $h_{1,2} = 1.5$ mm w.r.t. to the GP, calculated from the full complex potential Ω of Eq. (C4). For comparison we included an M-curve for both wires on the same side of the GP, one of them placed at $x = 0$.

IV. Common mode to differential mode coupling

The DM circuits on a PCB may generate a CM current which flows along the cables connected to the PCB. We consider the reciprocal setup, a CM current I_{CM} through the GP which arrives through a second plane such as a cabinet panel (CP) may provide (Fig. 9). The CM current distribution and the Z_t with respect to the DM circuit is calculated. Several limiting situations can be considered: the CP a) has a certain width $2p$ or b) is very large in the x-direction; the CP is c) nearby ($h_{CP}/w \ll 1$) or d) at a large distance from the GP ($h_{CP}/w \to \infty$). In the experiments we used a brass plate as CP of thickness $d_p = 1.5$ mm and width $2p = 20$ cm. We assume the thin plate limit for both CP and GP. The CP is usually larger than the GP. Induction currents reduce the magnetic field through the CP already at low frequencies; edge effects and skin effect are less important. Most calculations were

performed by the MOM. The sensing wire 1 is again placed at the distance $h_1 = 1.5$ mm from the GP ($2w = 5$ cm).

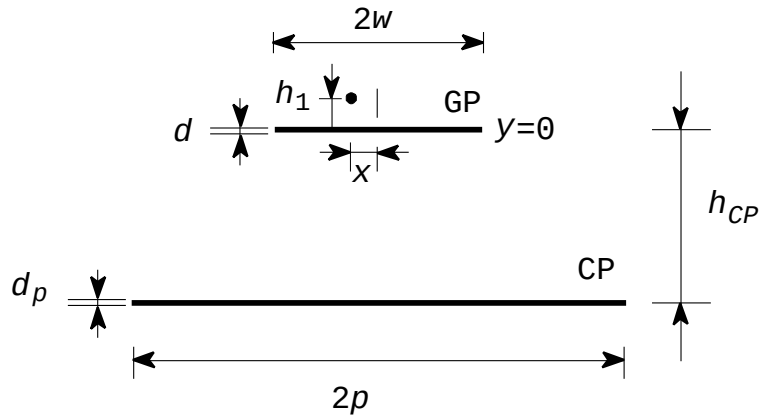

Fig. 9. Parameters for the PCB above a cabinet panel (CP).

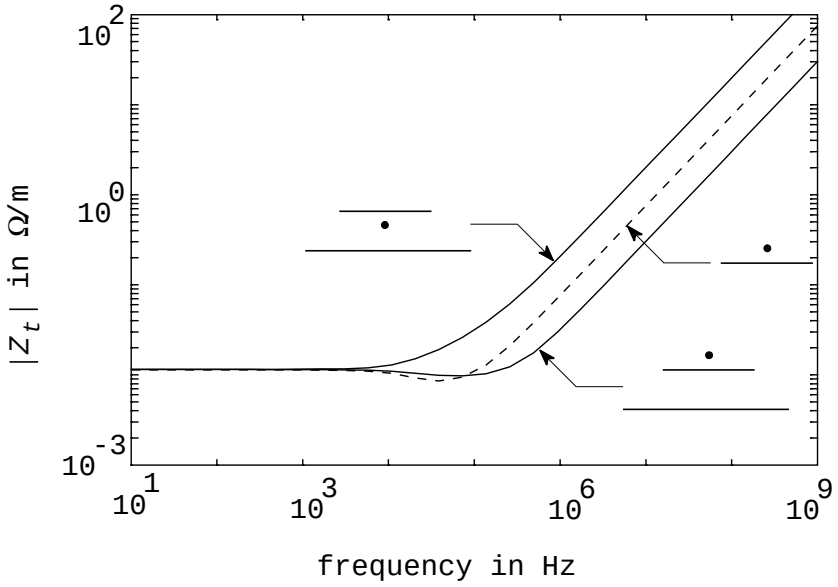

Fig. 10. CM to DM Z_t when the CP is far away (- - -), or at $h_{CP} = 1$ cm distance from the GP (—). The track is at 1.5 mm above or under the GP.

First we consider the CP at a large distance from the GP (see Fig. 10). At d.c. or low frequencies $K_z = I_{CM}/2w$ holds and $Z_t = R_\square/2w$ is equal to the d.c. resistance of the GP. Above a frequency f_c given by $2wd \simeq \delta^2$ [22] the current density $K_z(x)$ adjusts to reduce the penetration of the magnetic field through the GP; $K_z(x = 0)$ decreases towards the high frequency value $I_{CM}/\pi w$ [9, p. 63]. For the GP width chosen, the corresponding decrease in Z_t by a factor $2/\pi$ does barely occur. At high frequencies Z_t becomes inductive; M was calculated by conformal transformations, Appendix C3, Eq. (C9) where the injection wire was placed at a large distance. We again compare the $M(x, y)$-values for the sensing wire 1

at $x = 0$ and at $|x| = w$:

$$M(0, h_1) \approx \frac{\mu_0}{2\pi} \frac{h_1}{w} \tag{21}$$

$$M(|x| = w, h_1) \approx \frac{\mu_0}{2\pi} \sqrt{\frac{h_1}{w}}. \tag{22}$$

These expressions for M present two bounds, and are accurate to within 10 percent for the track at either side of the GP when $h_1/w < 0.9$.

Secondly, we place the 20 cm wide CP at the distance $h_{CP} = 1$ cm under the GP, a typical value often encountered in practice. The Z_t for several positions of the sensing wire 1 calculated by MOM is given in Fig. 10. Examples of magnetic field lines are shown in Fig. 11.

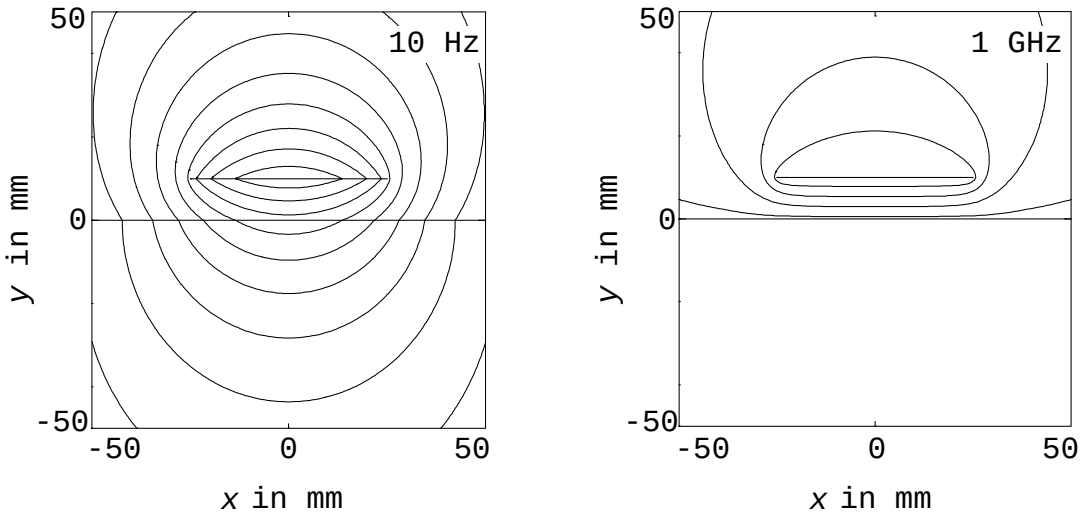

Fig. 11. Magnetic field pattern at low and at high frequency for a CM current through the CP ($2p = 20$ cm) which returns via the GP ($2w = 5$ cm).

At high frequencies the nearby CP ($h_{CP}/w \ll 1$) causes a homogeneous H-field under the GP and a strongly reduced field above the GP. The Z_t now depends on which side the sensing wire is placed. Because of the homogeneity of the field under the GP, a first approximation for $M(x, y)$ at $x = 0$ and $y = -h_1$, assuming $h_{CP}/w \ll 1$, is:

$$M(0, -h_1) \approx \mu_0 \frac{h_1}{2w}, \tag{23}$$

a factor π larger than Eq. (21) for the isolated PCB.

At other positions of the track 1 the M-values are more difficult to obtain. In principle, the magnetic field and M can be calculated by means of conformal transformation. Love [10] gave the general Schwarz-Christoffel transformation consisting of elliptic functions; his results were extended by Langton [23] and Lin [24]. This method only gives an implicit solution. For the position $(x, y) = (0, h_1)$ above the GP, expansion of the elliptic functions (Appendix C4) results in

$$M(0, h_1) \approx \mu_0 \frac{h_1 h_{CP}}{\pi w^2} \tag{24}$$

which is a factor $2h_{CP}/\pi w$ smaller than the M at the lower side of the GP, Eq. (23). For other positions, e.g. at the edge of the GP $|x| = w$, we proceed in a different and approximate way. For $h_{CP} \ll 2w$ the other edge may be thought infinitely far away. The H-field near one edge can then be derived from a simpler transformation which is often employed for the fringing field of a parallel plate capacitor [7, Sect. 7.7]. The solution is still implicit (see Appendix C5), but involves only an exponential. For $h_1 \ll h_{CP}$ the first two terms in the expansion of the exponential result in:

$$M(|x| = w, |y| = h_1) \approx \frac{\mu_0}{2w}\sqrt{\frac{h_1 h_{CP}}{\pi}} \tag{25}$$

irrespective on which side of the GP track 1 is placed. Already for $h_1 \simeq h_{CP}/10$ higher order terms in the expansion become discernible. A numerical fit to the calculations resulted in a correction term

$$\Delta M(|x| = w, y) \approx \frac{\mu_0}{2w} c_1 y \tag{26}$$

with $c_1 \simeq -1/3$, in which y is positive for positions above the GP. This ΔM restores the actual asymmetry between upper and lower positions of the track 1; for a more elaborate fit see Appendix C5 and Fig. C4. The variation of $M(x, h1)$ and $M(x, -h1)$ over the width of a GP is shown in Fig. 12a, whereas Fig. 12b gives the M as function of h_{CP}/w for a few fixed positions of the sensing wire. For this GP size and position ($2w = 5$ cm, $h_{CP} = 1$ cm) the assumption $h_{CP}/w \ll 1$ is not fulfilled, and the actual magnetic flux between GP and CP is lower than assumed. The current distribution $K_z(x)$ in the GP and the total flux between GP and CP calculated by MOM agreed well with the analytical expression for parallel strips given by Kuester and Chang [25, Eq. 6]. For wire 1 close to the GP, we corrected the M-values given above by the ratio of the total flux given in [25] and the flux of a assumed homogeneous field $\mu_0 I_{CM} h_{CP}/2w$; see Appendix C5 at the end.

V. Influence of the CP on the DM to DM crosstalk

When the cabinet panel approaches the ground plane, the magnetic field due to the DM circuit induces a circulating current in the CP even without net current flow in the CP. The DM to DM crosstalk depends on the position of the CP. For a disconnected CP, Fig. 13a shows the Z_t(1-2) at several h_{CP}, with both tracks at mid GP ($x_1 = x_2 = 0$). We again assumed $h_1 = h_2 = 1.5$ mm and $2w = 5$ cm.

Of course the Z_t at d.c. does not depend on the presence of the disconnected CP. At mid frequencies, region 3 of Fig. 3a, the Z_t is only reduced when track 2 is very close to the CP. The Z_t assumes the behavior of an isolated PCB already for distances h_{CP} of 1 cm. At high frequencies the field lines wrapping around the GP dominate the Z_t. For smaller distances h_{CP} the H-field under the GP is compressed, leading to higher M-values. The homogeneity of the field improves, and the M-values for $x_2 = 0$ and $|x_2| = w$ (lowest two curves in Fig. 13b) converge. At $h_{CP} = 1.5$ mm these M's are equal since both DM circuits then capture all magnetic flux under the GP. The field lines at the edges (see e.g. Fig. 11) show less curvature for smaller h_{CP}, as is demonstrated by the lower M for the sensing track above the GP.

We now connect the GP to the CP over their full width at both ends. A current I_{CM} flows in the closed CM loop, induced by I_1 in the DM circuit formed by wire 1 and the GP.

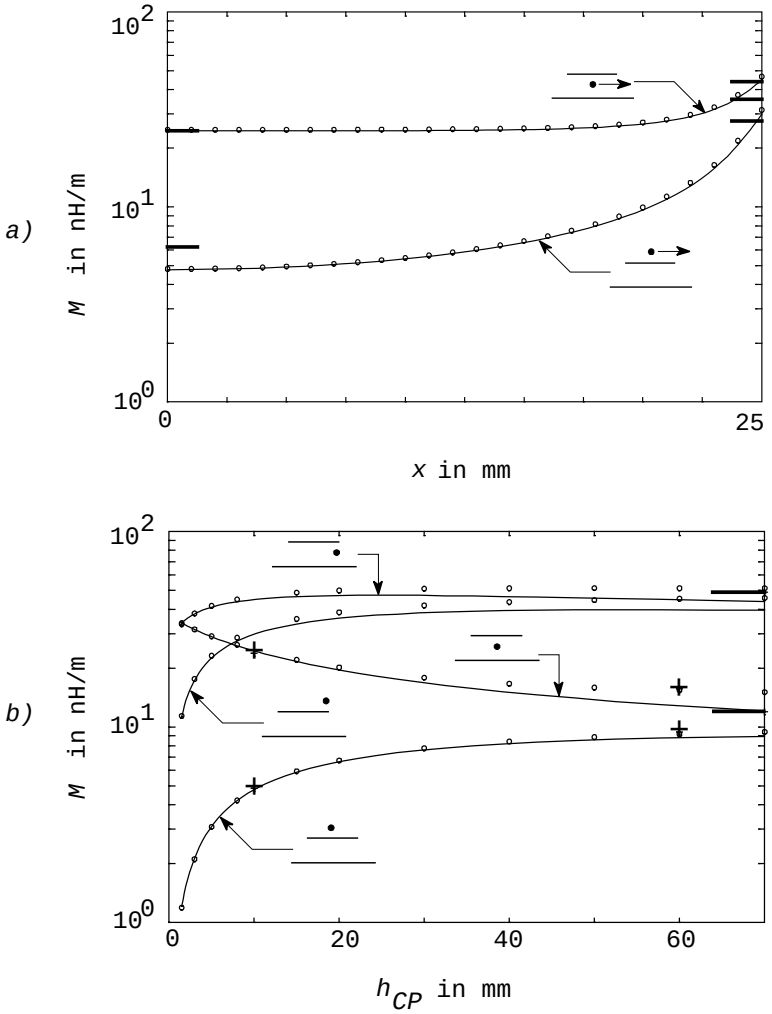

Fig. 12. a) Mutual inductance M between CM and DM loop when the x-position of the track varies over the GP (full width 5 cm). The 20 cm wide CP is at $h_{CP} = 1$ cm under the GP. The circles are MOM results, the solid lines are analytical approximations discussed in Appendix C5. The three markers on the right ordinate indicate the M-values at the edge. The middle one is M from Eq. (25), to which the correction ΔM from Eq. (26) has been added or subtracted. The markers on the left ordinate correspond to Eq. (24) and Eq. (23) without further correction. b) Mutual inductance M between CM and DM loop as function of h_{CP} for four positions of the sensing track. The measurements (Sect. VII) at $h_{CP} = 1$ cm and 6 cm are indicated (+). The upper marker at the right ordinate corresponds to Eq. (22), the lower to Eq. (21).

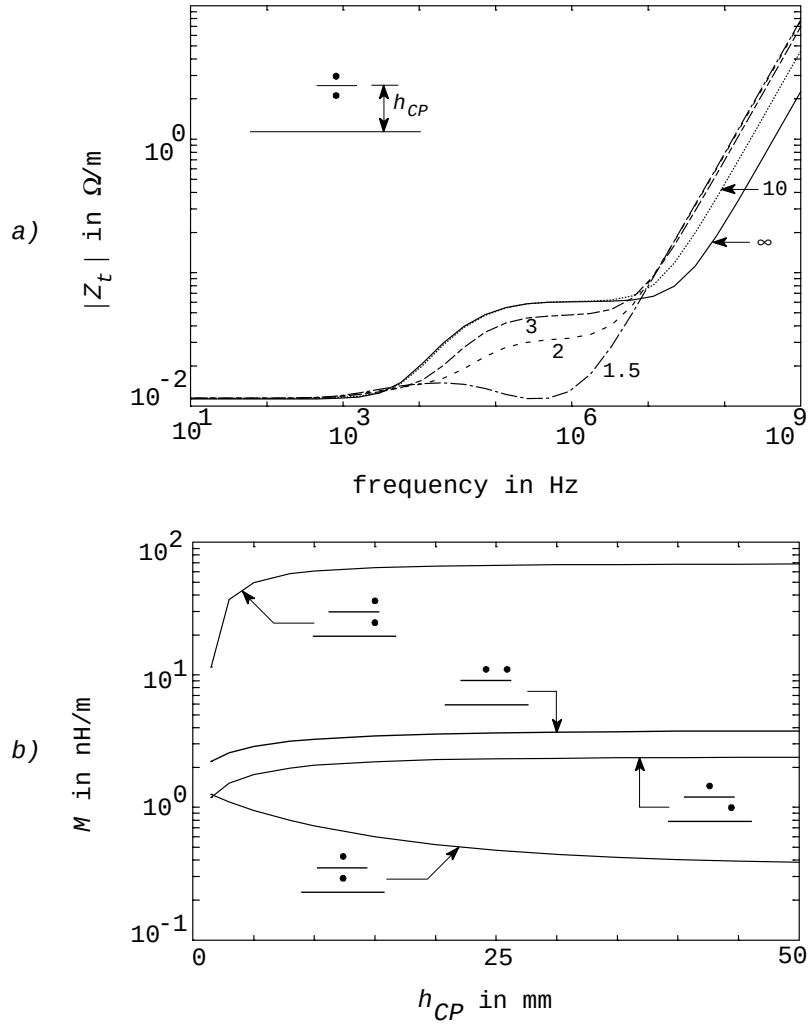

Fig. 13. a) DM to DM Z_t for several distances h_{CP} (in mm) between GP ($2w = 50$ mm) and CP ($2p = 20$ cm). b) M-part of Z_t for DM to DM, as function of h_{CP} for several positions of the injection and sensing tracks.

Both DM and CM loop couple via the transfer impedance Z_t(1-CM), given in the previous Section (see Fig. 10) for the reciprocal situation CM-1. We have

$$I_1 Z_t(\text{1-CM}) + I_{CM} Z_{CM} = 0, \quad \text{with} \quad Z_{CM} = R_{CM} + j\omega L_{CM}. \tag{27}$$

The selfinductance of the CM loop L_{CM}, as well as the distribution of I_{CM} over the GP and CP can be calculated by the MOM, which agreed with the analytical approximations of Kuester and Chang [25]. The R_{CM} is the series resistance of GP and CP. The final transfer impedance between the tracks 1 and 2 is denoted by Z_t(1-2,c) where c indicates the closed CM loop:

$$Z_t(\text{1-2,c}) = Z_t(\text{1-2,o}) - \frac{Z_t(\text{1-CM}) Z_t(\text{2-CM})}{Z_{CM}} \tag{28}$$

with Z_t(1-2,o) the transfer impedance in case of an open CM loop. Figure 14 shows Z_t(1-2,c), assuming a CP of 1.5 mm brass in which the skin effect is neglected, $h_{CP} = 1$ cm, $h_1 = h_2 = 1.5$ mm and $2w = 5$ cm.

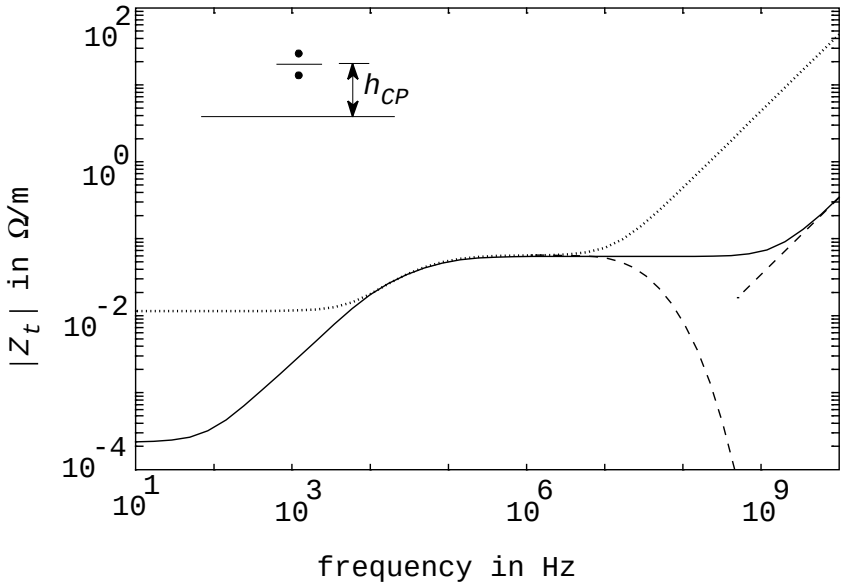

Fig. 14. The MOM results of the DM to DM Z_t (—) when the CP ($2p = 20$ cm) is connected to the GP ($2w = 50$ mm) at both ends; $h_{CP} = 1$ cm. Also indicated are the Z_t for a disconnected CP ($\cdots$), as well as the expected behavior due to the skin effect and due to the residual M-coupling (- - -).

Major changes occur at low frequencies; the small resistance R_{CP} of the CP is parallel to R_{GP} of the GP, and $Z_t = R_{GP}R_{CP}/(R_{GP} + R_{CP})$. However, already at 100 Hz the Z_t rises. In order to estimate the cross-over frequency from Eq. (28), one may replace Z_{CM} by $R_{CM} + j\omega L_{CM}$ and substitute both Z_t(1-CM) and Z_t(2-CM) by R_{GP}. In first approximation Z_t(1-2,o) also equals R_{GP}. The resulting cross-over frequency becomes $L_{CM}/2\pi R_{CP}$, which for our setup is 230 Hz. The small inductive component in Z_t(1-2,o) is mainly responsible for the lowering of the cross-over to about 100 Hz as apparent from Fig. 14. The flat region 3 is extended to higher frequencies. The short circuited CM loop reduces the flux and decreases the M-coupling. The dotted lines indicate the residual M-coupling, as well as the expected decrease due to the skin effect in the GP.

VI. A DM track between two planes

In multilayer PCB's the coupling of a signal track is reduced when the track is placed between two planes, ground and/or power; assume the planes at $y = \pm h_{PP}$ (Fig. 15). We first describe the Z_t between a track on top of a very wide PCB and a track midway between both planes at $(x_1, y_1) = (0, 0)$ carrying a current I_1. Assuming very wide GP's and filamentary wires for the tracks, the current distribution K_z in both planes can be calculated as in Sect. III, see Appendix A3. The 'thin plate' result is:

$$K_z(x) = -\frac{j\omega\mu_0 I_1}{2\pi R_\square}\int_0^\infty \frac{\cos(\alpha x)\,\mathrm{e}^{-\alpha h_{PP}}}{\alpha + j\beta(1+\mathrm{e}^{-2\alpha h_{PP}})}\,\mathrm{d}\alpha, \tag{29}$$

with $\beta = \omega\mu_0/2R_\square$ again. The high frequency K_z becomes

$$K_z(x) = -\frac{I_1}{4h}\mathrm{sech}\frac{\pi x}{2h_{PP}}, \tag{30}$$

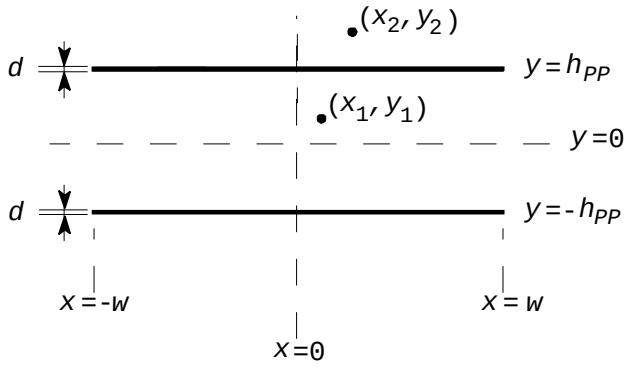

Fig. 15. Parameters for a wire 1 between two planes of width $2w$. The sensing wire 2 resides outside the two planes.

which is a factor $\pi/4$ smaller than the current density at $x = 0$ with only one GP; compare Eq. (3). The current density is also more concentrated near wire 1. For the 'thin plate' Z_t of a wire at (x_2, h_2) with $h_2 \geq h_{PP}$

$$Z_t = \frac{j\omega\mu_0}{2\pi} \int_0^\infty \frac{\cos(\alpha x_2)\, \mathrm{e}^{-\alpha h_2}}{\alpha + j\beta(1 + \mathrm{e}^{-2\alpha h_{PP}})}\, \mathrm{d}\alpha, \tag{31}$$

which describes regions 0, 2, and 3 in Fig. 16. We include the skin effect (region 3 and 4 in Fig. 16) to obtain the high frequency Z_t:

$$Z_t = \frac{R_\square}{\pi} \frac{kd}{\sinh kd} \int_0^\infty \frac{\cos(\alpha x_2)\, \mathrm{e}^{\alpha(d-h_2)}}{1 + \mathrm{e}^{-2\alpha h_{PP}}}\, \mathrm{d}\alpha. \tag{32}$$

The integral can be expressed in elementary Ψ-functions [26, 3.541.6]. For $(x_2, y_2) = (0, 2h_{PP})$ and $d \downarrow 0$ the integral is simply $(\ln 2)/2h_{PP}$. In the flat region 3 Z_t is a factor $\ln 2$ smaller than the Z_t with one GP, Eq. (8), at the equivalent position. However, because a part of the current returns at the other side of wire 1, the reduction in Z_t is less than 1/2 as could be expected naively.

When the injection wire is midway between the planes, the return current is shared equally by both planes. For other y-position of the wire, the total current varies linearly as $-(h_{PP} + y)I_1/2h_{PP}$ for the top and as $-(h_{PP} - y)I_1/2h_{PP}$ for the bottom plane at high frequencies.

The M-part in Z_t is strongly reduced since both planes effectively confine the magnetic field. An approximate procedure again has been followed assuming that wire 1 and 2 are at some distance $|\delta x_1|$ and $|\delta x_2|$ from the edge of the PCB; see Appendix C6. For M one finds:

$$M = \frac{\mu_0\, \delta h_2}{2\pi} \left(\frac{h_{PP}}{\pi |\delta x_2|^3} \right)^{\frac{1}{2}} \mathrm{e}^{-\frac{\pi |\delta x_1|}{2h_{PP}} - \frac{1}{2}}, \tag{33}$$

where δh_2 is the vertical distance of wire 2 above the top plane. Because of the exponential in δx_1 only one edge is taken into account. In Fig. 17 we compare Eq. (33) with the complex potential result of Eq. (C25). When wire 1 is deeply buried between both planes at large δx_1, very low M-values result by Eq. (33) and other effects may become dominant. Assume for instance that the planes provide of ground and d.c. power; insufficient decoupling between

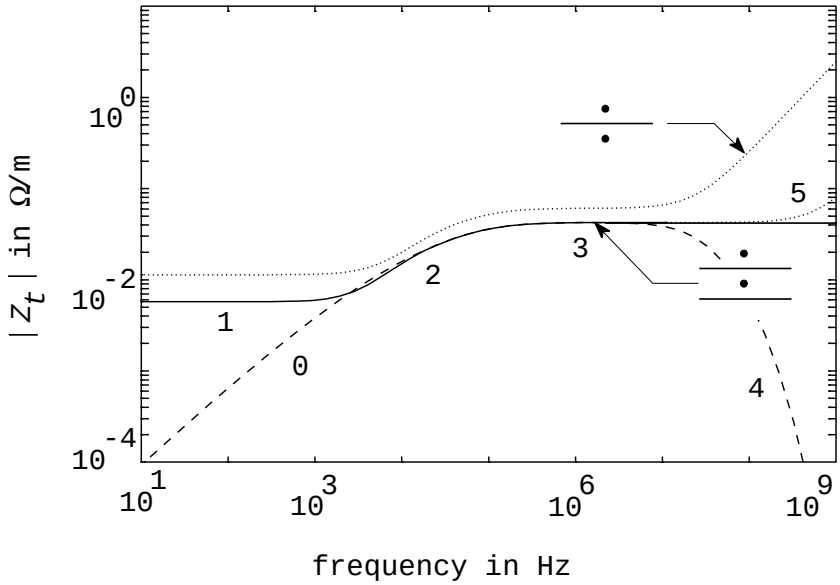

Fig. 16. General behavior of $|Z_t|$ between track 1 and 2 with $2w = 5$ cm wide planes. Track 1 is positioned at the origin, while track 2 resides at $(0, 2h_{PP})$, width $h_{PP} = 1.5$ mm. The solid curve 1-2-3-5 has been calculated by means of MOM; the deviation in region 5 is due to numerical errors. The curve 0-2-3-4 (- - -) shows $|Z_t|$ for very wide planes; the skin effect again lowers the impedance in region 4. For comparison we have included the behavior for a PCB with only one GP.

the planes at the ends may cause a different return current $-(\frac{1}{2} \pm a)I_1$ through the top (+) and bottom (−) plane. The value of a has to be estimated for an actual PCB; here we just assume any value $0 \leq |a| \leq \frac{1}{2}$. In worst case, no net return current flows through either of the planes. This situation is comparable to Section IV for a 'CM' current $a\, I_1$; the results of Eqs. (24) and (25) can be multiplied by a, with h_{PP} substituted for h_{CP}.

VII. Measurements

The three layer PCB (Fig. 1) consisted of a single and a double layer PCB firmly pressed against each other. On each side of the GP two 1.5 mm wide tracks (Fig. 1) were placed at $s = 10$ mm apart. Brass plates (30×20 cm^2) at both ends of the combined PCB minimized distortion of the 2D-fields due to end-effects. SMA-connectors with low proper Z_t were mounted in one of the brass plates (A in Fig. 1). In order to avoid Z_t-contributions from the cables and the measuring equipment, the brass plate A was properly connected to the backpanel of an EMC-cabinet [27] in which the measuring equipment resided. The cables were RG223 with double braided shield; several ferrite cores kept the CM currents through the cables sufficiently low.

Between 10 Hz and 100 kHz a sinewave generator provided the injection current which was measured by an active current probe. The generator was placed outside the EMC-cabinet. A lock-in detector inside that cabinet determined the DM voltage in amplitude and phase; see e.g. [28]. The output of the current probe served as reference. Between 200 kHz and 1 Ghz we employed a spectrum-network analyzer; the tracking generator provided the injection current. Up to 50 MHz an inductive current probe measured the current directly at the input connector on the brass plate A. Above 50 MHz an S-parameter set was used to determine the injection

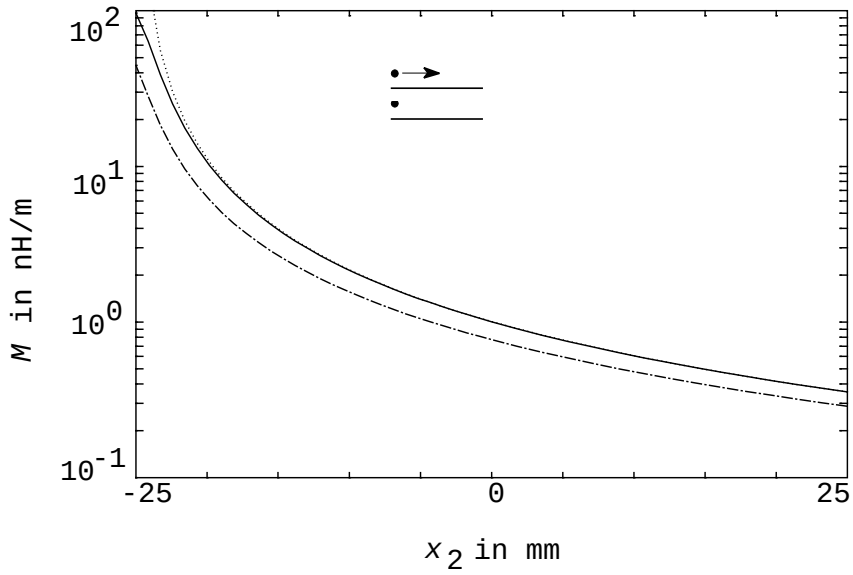

Fig. 17. The mutual inductance part M of Z_t between two DM circuits. The injection wire resides between the two finite planes, near the edge. The sensing wire at the upper plane moves over the full width. The full expression Eq. (C24) (—) as well as the approximations Eqs. (33) $(\cdots)$ and (C25) $(-\cdot-\cdot-)$ are shown

current at the input SMA connector of the PCB.

We present measurements of DM-DM crosstalk which demonstrate the current distribution. Figure 18 shows the Z_t for an isolated PCB with current injection in track 1, and track 2 and 4 as sensing tracks (see Fig. 1). Up to 70 MHz measurements and calculations agree. The current contraction under track 1 (region 3 in Fig.3a) causes $|Z_t(1\text{-}2)|$ to rise and $|Z_t(1\text{-}4)|$ to decrease. The M-coupling (region 5) is nearly the same for track 2 and 4, as indicated by the convergence of the Z_t curves above 10 MHz. The frequency of the resonance peaks in Z_t agree with standing waves in injection and sensing circuit over the length $\ell = 0.2$ m: $\ell = (2n+1)\lambda/4$ with $n = 0, 1, 2, ...$ Here λ is the wavelength calculated with an effective dielectric constant $\varepsilon_{r,eff} = 3.41$ [7, Sect. 8.6]. For this slender GP the skin effect does barely show up because of the predominant M-coupling and because of the resonances.

The Z_t for one or both tracks at the edge of the GP is shown in Fig. 18b. The width of the GP is $2w = 15$ cm. Here too, measurements and calculations agree up to the resonances.

The measured and calculated CM to DM crosstalk is presented in Fig. 19 for the mid position of the sensing track. The current was injected in the CM loop through the CP, and returned through the 5 cm wide GP. Two distances h_{CP} of 1 cm and of 6 cm were used. The experimental M-values are included in Fig. 12. Standing waves occur as in the DM-DM crosstalk. The frequency of the low-Q shoulder on the first peak varies with h_{CP}. This resonance probably originates in the current injection circuit.

VIII. Conducted emission

We apply the transfer impedance Z_t(DM-CM) to describe the emission due to a CM current through a cable connected to the model PCB. The current waveform in the DM circuit are typical choices for a switched-mode power supply and for several families of logic circuits

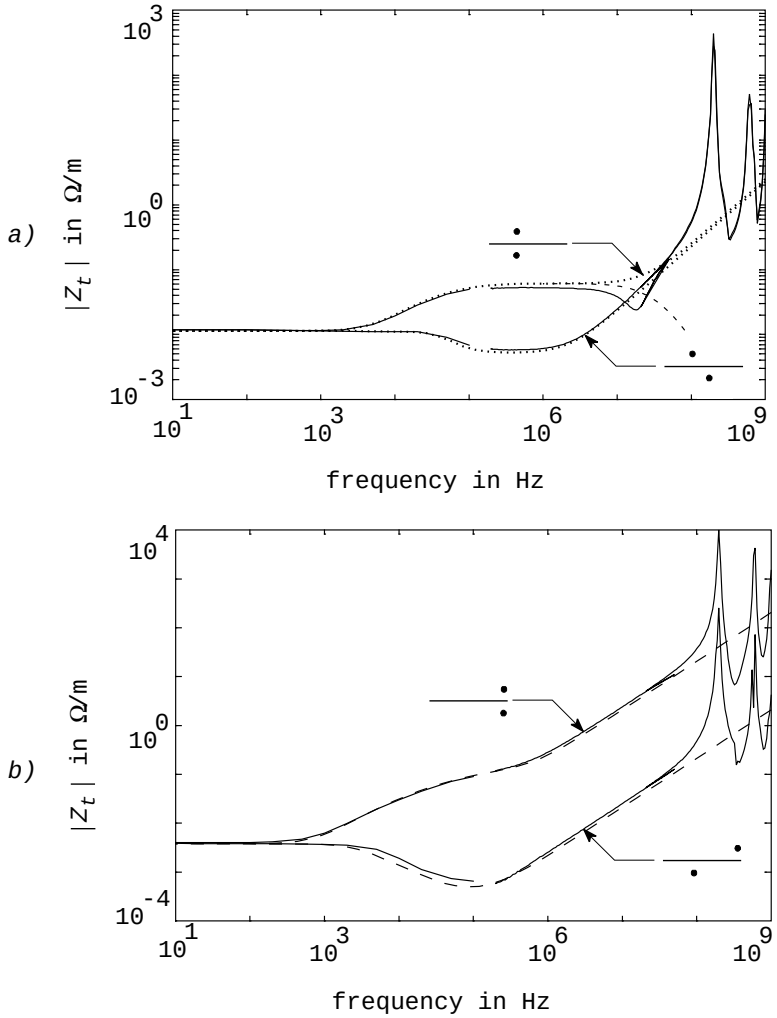

Fig. 18. a) The measured DM to DM $|Z_t(1\text{-}2)|$ and $|Z_t(1\text{-}4)|$ (—) together with the MOM calculations $(\cdots)$. Tracks 1 and 2 are on opposite sides at 5 mm from the middle line of the GP ($2w = 5$ cm); the x-distance between track 1 and 4 is $s = 10$ mm. The resonances above 100 MHz are discussed in the text. The actual reduction of $|Z_t(1\text{-}2)|$ due to the skin effect occurs at lower frequencies than expected (- - -), because of the opposite phase in the couplings by the skin effect and by the inductive M-coupling, see e.g. Kaden [9, Fig. 171]. b) Measured (—) and calculated (- - -) DM to DM $|Z_t|$ with one or both tracks at the edge of the GP ($2w = 15$ cm).

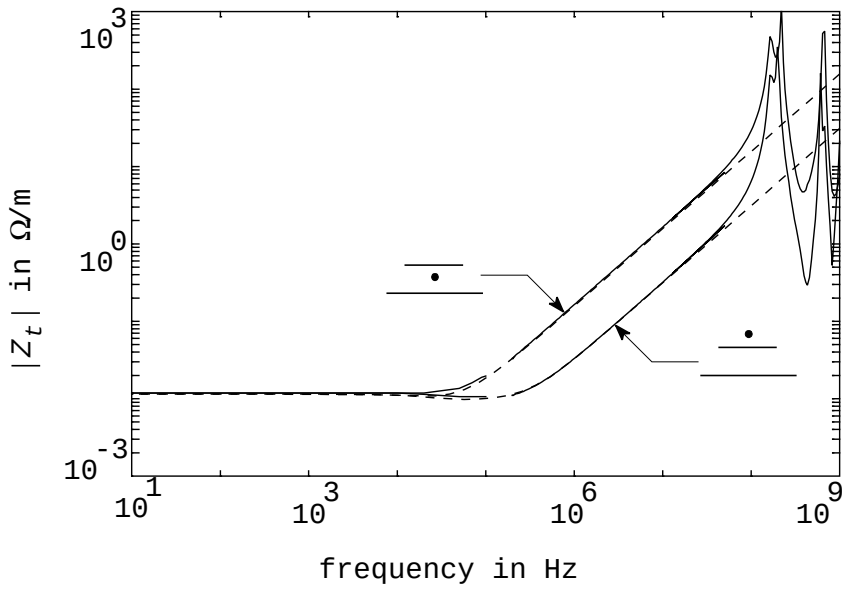

Fig. 19. Measured (—) and calculated (- - -) CM to DM Z_t for two positions of the sensing track; $h_{CP} = 1$ cm, $2w = 50$ mm, $h_1 = 1.5$ mm.

(Fig. 20). In the model we connect the GP at one side to the CP (inset Fig. 21). The cable is represented by a half wave antenna with a radiation resistance $R_0 = 150\ \Omega$. This resonance condition may not occur at all frequencies in the DM signal, but will most probably do so at some frequency for which the emission limits might then be exceeded. When propagation delays over the PCB are neglected, the induced CM voltage $v^{ind}(t)$ can be imagined as a localized source between cable and GP which drives the cable as antenna. The CM current $i_{CM}(t)$ through the cable at resonance is then given by $v^{ind}(t)/R_0$.

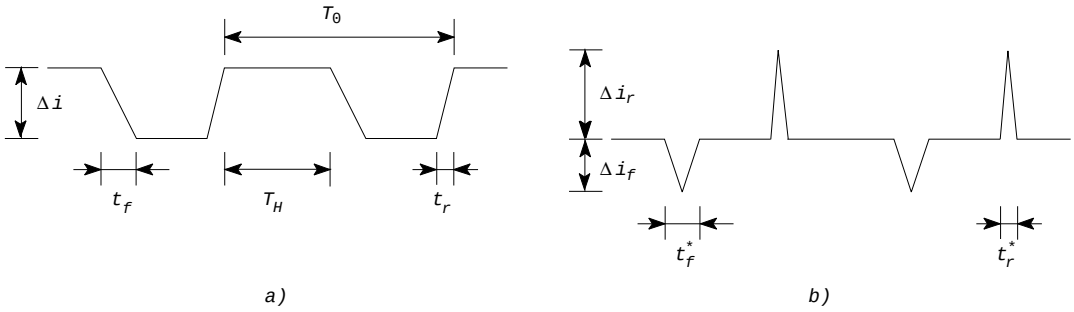

Fig. 20. Typical current waveforms for *a*) switched-mode power supplies and TTL and ECL digital circuits, *b*) for fast CMOS circuits.

The DM current waveforms in switched-mode power supplies or TTL and ECL digital circuits is approximated by the trapezoids in Fig. 20a. For CMOS and similar circuits, the DM current resembles more a triangular shape (Fig. 20b). The trapezoidal current $i_{DM}(t)$ is

expanded in the Fourier series

$$i_{DM}(t) = \sum_{n=-\infty}^{\infty} I_n^{DM} e^{jn\omega_0 t}, \tag{34}$$

with $\omega_0 = 2\pi f_0 = 2\pi/T_0$. For $t_r = t_f = \tau$ the coefficients I_n^{DM} are given by

$$I_n^{DM} = \Delta i \frac{\sin(n\omega_0\tau/2)}{n\omega_0\tau/2} \frac{\sin[n\omega_0(T_H+\tau)/2]}{n\pi}. \tag{35}$$

The transfer impedance Z_t(DM-CM) can be approximated by

$$Z_t(\omega) \approx R_{GP} + j\omega M. \tag{36}$$

The induced voltage $v^{ind}(t)$ then follows from

$$v^{ind}(t) = \sum_{n=-\infty}^{\infty} V_n^{ind} e^{jn\omega_0 t}, \tag{37}$$

with

$$V_n^{ind} = Z_t(n\omega_0) I_n^{DM}. \tag{38}$$

According to the EN55022 regulation, the maximum electric field strength should not exceed 30 dBμV/m (at 10 m for class B equipment) in the frequency range 30-230 MHz. This requires a CM current through the cable of less than 3 μA, see e.g. Ott [29] or Goedbloed [30, Sect. 2.4.1].

The fundamental frequency f_0 determines the minimal harmonic number m in Eq. (34) for which the EMC requirements should be met. The corresponding spectral component of $i_{CM}(t)$ is $I_m^{CM} = V_m^{ind}/R_0$ when the resistance term in Z_t is neglected. The upper bound for the amplitude of this spectral component is given by

$$|I_m^{CM}| \leq \frac{4M\,\Delta i}{\pi m R_0 \tau}, \tag{39}$$

which hold for the waveform given in Fig. 20a. For the waveform given in Fig. 20b, τ must be replaced by $\min\{t_r^*/2, t_f^*/2\}$ and Δi by $\max\{\Delta i_r, \Delta i_f\}$.

In Table I, $|I_m^{CM}|$ is given for a few families of digital circuits. As can be seen, the 3 μA limit for ECL3 and HLL digital logic requires extensive EMC measures. A reduction of about 44 dB and 65 dB respectively should be obtained in case of our 0.2 m long and 5 cm wide PCB, for instance by an extra ground plane or cabinet panel, smaller distances between tracks and GP, filter connectors, etc.

We tested these calculations in a setup which is often used for precompliance measurements [31], see Fig. 21. The CM current is generated by the DM circuits above (track 1, Fig. 1) or under (track 2) the GP. This CM current is measured at the 150 Ω load, formed by the 100 Ω SMD-resistor and the 50 Ω impedance of the cable connected to the spectrum analyzer. For our 5 cm wide and 20 cm long PCB, the ratio of the DM and CM currents is given in Fig. 21, measured as well as calculated.

Table I. Upper bounds for the maximal spectral components of i_{CM} given by the r.h.s. of Eq. (39). For the switched-mode power supply (SMPS) and ECL3 (or ECL-100K) digital logic, the trapezoidal waveform (Fig. 20a) is used; a triangular shape form (Fig. 20b) is assumed for CMOS and HLL logic. The mutual inductances M are calculated by MOM (Sect. IV.).

TYPE $f_0/\tau/\Delta i$	$\max\{\lvert I_m^{CM}\rvert\}$ in μA per length of PCB			
	$2w = 5$ cm		$2w = 15$ cm	
	injection 1 $M = 4.8$ nH/m	injection 2 $M = 24.9$ nH/m	injection 1 $M = 0.6$ nH/m	injection 2 $M = 10.6$ nH/m
SMPS 100 kHz/100 ns/1 A	1.4	7.0	0.2	3.0
ECL3 (ECL-100K) 230 MHz/1.3 ns/14.8 mA	463.9	2406.2	58.0	1024.3
CMOS 10 MHz/60 ns/4.2 mA	2.9	14.8	0.4	6.3
HLL (CMOS 3V) 230 MHz/1.5 ns/100 mA	5432.5	28181.0	679.1	11996.7

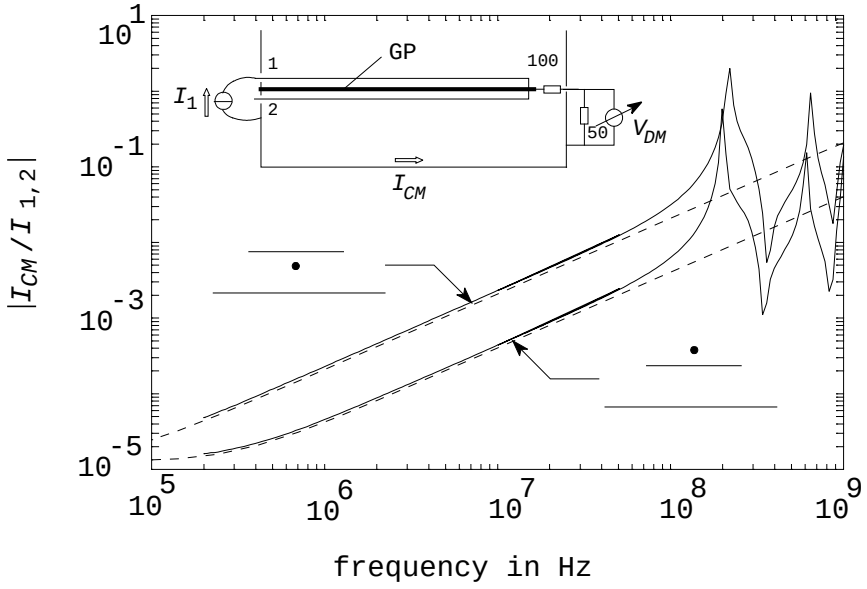

Fig. 21. Measured (—) and calculated (- - -) current transfer between DM and CM circuits, for a DM injection track above (1) or below (2) the GP. The inset shows the setup for precompliance measurements with current injection through track 1. The CM current is measured via the 150 Ω load.

IX. Concluding remarks

The M-part in the DM to DM crosstalk shows a strong dependence when one or both tracks are near the edges of the GP. A distance of $3h_1$ reduces the crosstalk by about one order of magnitude. For distances h_{CP} of 1 cm and more between GP and CP, the influence of the CP on this cross-talk nearly vanishes.

When a CP is present under the GP, the M-part of the CM to DM crosstalk is lowest for traces at the upper side of the GP. Even for our slender PCB this difference is about one order of magnitude. For traces at the edges the difference between upper and lower side is smaller.

In our analysis we used 1.5 mm thick insulation. Many multilayer PCB have also interlayer insulations of 0.2 mm, and correspondingly smaller tracks and track distances. There is also a tendency to reduce the copper layer thickness. For such PCB's the analytical expressions for Z_t are valuable.

In a PCB with more than one ground plane or power plane the DM return current will be shared by those planes. A 2D analysis of such sharing can be carried out in a similar way as presented. The current distribution also depends on the action of e.g. the logical circuits, whether they switch the signal lead to ground or to power. The position of decoupling capacitors between the planes is then also important.

Appendix A

1. Carson's approach

A filamentary wire 1 is positioned at $x = 0$ in a dielectric region at the height h_1 above conductive ground which fills the lower halfspace $y < 0$ (Fig. 6a). The wire carries a current wave I_1 propagating as $\mathrm{e}^{j\omega t-\gamma z}$ in the positive z-direction. The propagation constant γ is taken small. The E_x and E_y components of the electrical field are neglected, as well as the displacement current in the ground. The equation

$$\nabla^2 E_z = j\omega\mu\sigma E_z \tag{A1}$$

holds for time harmonic fields in the GP. Under the assumptions mentioned Carson's solution [13] of Eq. (A1) is the Fourier cosine integral w.r.t. x

$$E_z(x,y) = -\int_0^\infty F(\alpha)\cos(\alpha x)\ \mathrm{e}^{y\sqrt{\alpha^2+j\omega\mu\sigma}}\,\mathrm{d}\alpha. \tag{A2}$$

The x and y-components of the magnetic field $\mathbf{H}$ in the ground stem from Maxwell's equation $\nabla\times\mathbf{E} = -j\omega\mu\mathbf{H}$, in which $\mu = \mu_0\mu_r$. Above ground the current I_1 produces the familiar r^{-1}-field $\mathbf{H}_1$ and the current distribution $J_z(x,y) = \sigma E_z(x,y)$ produces a magnetic field $\mathbf{H}_2$ with transverse components only. Expand both magnetic fields in Fourier cosine integrals (x-components) and Fourier sine integrals (y-components):

$$\begin{aligned} H_{1x} &= \frac{I_1}{2\pi}\frac{h_1-y}{x^2+(h_1-y)^2} \\ &= \frac{I_1}{2\pi}\int_0^\infty \cos(\alpha x)\,\mathrm{e}^{-\alpha(h_1-y)}\,\mathrm{d}\alpha, \\ H_{1y} &= \frac{I_1}{2\pi}\frac{x}{x^2+(h_1-y)^2} \\ &= \frac{I_1}{2\pi}\int_0^\infty \sin(\alpha x)\,\mathrm{e}^{-\alpha(h_1-y)}\,\mathrm{d}\alpha, \end{aligned} \tag{A3}$$

$$\begin{aligned} H_{2x} &= +\int_0^\infty [\phi(\alpha)+\frac{I_1}{2\pi}\,\mathrm{e}^{-\alpha h_1}]\cos(\alpha x)\,\mathrm{e}^{-\alpha y}\,\mathrm{d}\alpha, \\ H_{2y} &= -\int_0^\infty [\phi(\alpha)+\frac{I_1}{2\pi}\,\mathrm{e}^{-\alpha h_1}]\sin(\alpha x)\,\mathrm{e}^{-\alpha y}\,\mathrm{d}\alpha. \end{aligned} \tag{A4}$$

In these Fourier integrals the values of y are restricted to negative values for the exponent, i.e. $y < h_1$ in Eq. (A3) and $y > 0$ in Eq. (A4). The second term between the braces in Eq. (A4) represents the image current at $y = -h_1$ which has been added for convenience. The boundary conditions for the magnetic fields and inductions at the plane $y = 0$ yields a linear system of equations, from which the unknown quantities $F(\alpha)$ and $\phi(\alpha)$ can be determined. The current distribution $J_z(x,y)$ in the GP becomes

$$J_z(x,y) = -\frac{j\omega\mu\sigma I_1}{\pi}\int_0^\infty \frac{\cos\alpha x}{\alpha\mu_r+\sqrt{\alpha^2+j\omega\mu\sigma}}\,\mathrm{e}^{-\alpha h_1}\,\mathrm{e}^{y\sqrt{\alpha^2+j\omega\mu\sigma}}\,\mathrm{d}\alpha. \tag{A5}$$

For nonmagnetic materials ($\mu_r = 1$) the integral Eq. (A5) is the same as given by Carson [13].

2. Ground plane of finite thickness

The GP is now a plate at $-d < y < 0$, still of infinite extent in the x-direction (Fig. 6b). Develop the electric field E_z in the GP in a Fourier cosine integral w.r.t. x

$$E_z(x,y) = -\int_0^\infty \left[F_+(\alpha)\,\mathrm{e}^{y\sqrt{\alpha^2+j\omega\mu\sigma}} \;+\; F_-(\alpha)\,\mathrm{e}^{-y\sqrt{\alpha^2+j\omega\mu\sigma}}\right]\cos(\alpha x)\,\mathrm{d}\alpha. \tag{A6}$$

The 'ansatz' for the magnetic fields $\mathbf{H}_1$ and $\mathbf{H}_2$ above the GP remain as above. The magnetic field $\mathbf{H}$ in the GP again stems from the Maxwell equation $\nabla\times\mathbf{E} = -j\omega\mu\mathbf{H}$. Below the GP we have to allow a magnetic field $\mathbf{H}_3$ which satisfies Laplace's equation:

$$\begin{aligned} H_{3x} &= \int_0^\infty \psi(\alpha)\cos(\alpha x)\mathrm{e}^{\alpha y}\,\mathrm{d}\alpha, \\ H_{3y} &= \int_0^\infty \psi(\alpha)\sin(\alpha x)\mathrm{e}^{\alpha y}\,\mathrm{d}\alpha. \end{aligned} \tag{A7}$$

The Fourier transforms of all these fields together with the boundary conditions at $y = 0$ and $y = -d$ yield a set of linear equations, from which $F_+(\alpha)$, $F_-(\alpha)$, $\phi(\alpha)$ and $\psi(\alpha)$ are determined. We have

$$F_+(\alpha) = +\frac{j\omega\mu I_1}{\pi}\frac{(\alpha\mu_r+\xi)\,\mathrm{e}^{-\alpha h_1}}{D} \tag{A8}$$

$$F_-(\alpha) = -\frac{j\omega\mu I_1}{\pi}\frac{(\alpha\mu_r-\xi)\,\mathrm{e}^{-\alpha h_1-2d\xi}}{D} \tag{A9}$$

$$\phi(\alpha) = -\frac{I_1}{\pi}\,\frac{\alpha\mu_r\,\mathrm{e}^{-\alpha h_1}\left\{(\alpha\mu_r+\xi)-(\alpha\mu_r-\xi)\,\mathrm{e}^{-2d\xi}\right\}}{D} \tag{A10}$$

$$\psi(\alpha) = +\frac{I_1}{\pi}\,\frac{2\alpha\mu_r\xi\,\mathrm{e}^{\alpha(d-h_1)-d\xi}}{D} \tag{A11}$$

$$D = (\alpha\mu_r+\xi)^2-(\alpha\mu_r-\xi)^2\,\mathrm{e}^{-2d\xi} \tag{A12}$$

with $\xi = \sqrt{\alpha^2+j\omega\mu\sigma}$. The current distribution in the GP becomes

$$\begin{aligned} J_z(x,y) &= \sigma E_z(x,y) \\ &= -\frac{j2\omega\mu\sigma I_1}{\pi}\int_0^\infty \frac{\alpha\mu_r\sinh\left[(d+y)\xi\right]+\xi\cosh\left[(d+y)\xi\right]}{(\alpha\mu_r+\xi)^2-(\alpha\mu_r-\xi)^2\,\mathrm{e}^{-2d\xi}}\cos(\alpha x)\,\mathrm{e}^{-(\alpha h_1+d\xi)}\,\mathrm{d}\alpha. \end{aligned} \tag{A13}$$

In the limiting case $d\to\infty$, this equation reduces to Eq. (A5) as it should. In the 'thin plate limit' we let $d\downarrow 0$ while keeping the sheet resistance $R_\Box = 1/\sigma d$ constant. The resulting sheet current density is Eq. (10). The Z_t between the injection wire and a sensing wire can be calculated according to Eq. (1) from the flux $\Phi(x)$ between the GP and the sensing wire and the electric field at the surface $E_z = J_z/\sigma$ close to the sensing wire; see Fig. 2. It is more convenient to introduce a flux function or vector potential A_z. We choose to write the electric

field $E_z(x,y)$ in the material as $-j\omega A_z(x,y)$ and require that A_z also correctly describes the magnetic field outside the GP:

$$A_z(x,y) = A_z^{dp}(x,y) + \mu_0 \int_0^\infty \cos(\alpha x)\,\frac{\phi(\alpha)}{-\alpha}\,\mathrm{e}^{-\alpha y}\,\mathrm{d}\alpha \qquad (y>0) \tag{A14}$$

with

$$A_z^{dp} = -\frac{\mu_0 I_1}{4\pi}\ln\frac{x^2+(y-h_1)^2}{x^2+(y+h_1)^2} \tag{A15}$$

and

$$A_z(x,y) = \mu_0 \int_0^\infty \cos(\alpha x)\,\frac{\psi(\alpha)}{\alpha}\,\mathrm{e}^{+\alpha y}\,\mathrm{d}\alpha. \qquad (y<0) \tag{A16}$$

The A_z^{dp} is the vector potential for a dipole of two line currents $\pm I_1$ placed at $y=\pm h_1$. Because of the applied boundary conditions for the magnetic fields, A_z is continuous at both surfaces of the GP. Because of the exponentials in y in Eqs. (A14) and (A16), the vector potential vanishes at large distances; the current I_1 fully returns through the GP. For Z_t we rewrite Eq. (1) as:

$$Z_t = j\omega A_z(x_s,y_s)/I_1 \tag{A17}$$

where (x_s,y_s) is the position of the sensing wire. In the thin plate limit the integrals in Eqs. (A14) and (A16) reduce both to

$$\int_0^\infty \frac{\cos(\alpha x)\mathrm{e}^{-\alpha h_t}}{\alpha+j\beta}\,\mathrm{d}\alpha = -\frac{\mathrm{e}^{j\beta h_t}}{2}\left[\mathrm{e}^{\beta x}\mathrm{Ei}(-\beta x - j\beta h_t) + \mathrm{e}^{-\beta x}\mathrm{Ei}(\beta x - j\beta h_t)\right], \tag{A18}$$

where $\beta = \mu_0\omega/2R_\square$ and $h_t = h_1 + h_2$, h_2 the distance between sensing wire and GP; this h_t should be used when wire 1 and 2 are on the same side as well as on opposite sides. Abramowitz [19] defines the exponential integral Ei only for positive real arguments, but by means of analytical continuation the same definition holds for general complex argument excluding the positive real axis; for positive real values the principal value of the definition integral must be used [19, Footnote 4 p. 228]. Bergervoet [32] obtained a similar result by a different method. The line dipole Eq. (A15) explains why the current density is sensed more directly by a wire at the opposite side of the GP. This is also shown by the field plots in Fig. 4a.

3. Injection wire between two plates

Suppose injection wire 1 is placed between two plates which are at $y=\pm h_{PP}$ and which have a thickness d. Here we proceed via the vector potential as described in the previous section. The Fourier coefficients for A_z are between both plates ($-h_{PP} < y < h_{PP}$ and $\mu_r = 1$)

$$A_z(\alpha) = \frac{\mu_0}{\alpha}[\phi_+(\alpha)\,\mathrm{e}^{\alpha y} + \phi_-(\alpha)\,\mathrm{e}^{-\alpha y}], \tag{A19}$$

outside both plates

$$A_z(\alpha) = \begin{cases} \dfrac{\mu_0}{\alpha}\psi_-(\alpha)\,\mathrm{e}^{-\alpha y} & y > h_{PP}+d \\[2ex] \dfrac{\mu_0}{\alpha}\psi_+(\alpha)\,\mathrm{e}^{\alpha y} & y < -(h_{PP}+d) \end{cases} \tag{A20}$$

and inside both plates

$$A_z(\alpha) = \mu_0[F_{i+}(\alpha)\,\mathrm{e}^{y\xi} + F_{i-}(\alpha)\,\mathrm{e}^{-y\xi}] \tag{A21}$$

with $\xi = \sqrt{\alpha^2 + j\omega\mu_0\sigma}$ and $i = 1, 2$ for the upper and lower plate respectively. The source term due to the current I_1 through wire 1 at $(0, y_1)$ is

$$\frac{\mu_0 I_1}{2\pi\alpha}\,\mathrm{e}^{-\alpha|y-y_1|}. \tag{A22}$$

Continuity of A_z and $\partial A_z/\partial y$ at the four surfaces $y = \pm h_{PP}$ and $y = \pm(h_{PP} + d)$ results in a set of equations. Of special interest are the solutions in case of wire 1 midway between the plates ($y_1 = 0$):

$$F_{1+}(\alpha) = F_{2-}(\alpha) = -\frac{I_1}{\pi}\,\frac{(\alpha-\xi)\mathrm{e}^{h_{PP}(\alpha-\xi)}}{D(\alpha)} \tag{A23}$$

$$F_{2+}(\alpha) = F_{1-}(\alpha) = +\frac{I_1}{\pi}\,\frac{(\alpha+\xi)\mathrm{e}^{h_{PP}(\alpha+\xi)+2d\xi}}{D(\alpha)} \tag{A24}$$

$$\psi_+(\alpha) = \psi_-(\alpha) = \frac{I_1}{\pi}\,\frac{2\alpha\xi\,\mathrm{e}^{\alpha(2h_{PP}+d)+d\xi}}{D(\alpha)} \tag{A25}$$

$$\phi_+(\alpha) = \phi_-(\alpha) = \frac{-j\omega\mu_0\sigma\,(\mathrm{e}^{2d\xi}-1)}{D(\alpha)} \tag{A26}$$

$$D(\alpha) = \mathrm{e}^{2\alpha h_{PP}}[\mathrm{e}^{2d\xi}(\alpha+\xi)^2 - (\alpha-\xi)^2] + j\omega\mu_0\sigma\,(\mathrm{e}^{2d\xi}-1). \tag{A27}$$

For the Z_t at (x_s, y_s) above the top plate ($y_s \geq h_{PP} + d$) we obtain

$$Z_t(x_s, y_s) = \frac{2j\omega\mu_0}{\pi}\int_0^\infty \frac{\cos(\alpha x_s)\,\mathrm{e}^{\alpha(2h_{PP}+d-y_s)+d\xi}}{D(\alpha)}\,\mathrm{d}\alpha. \tag{A28}$$

Appendix B

A current I_1 flowing in the positive z-direction through a filamentary wire at $\mathbf{r}_1 = (x_1, h_1)$ (Fig. 6c) generates the vector potential at $\mathbf{r} = (x, y)$

$$A_z^{(1)}(\mathbf{r}) = -\frac{\mu_0 I_1}{2\pi} \ln|\mathbf{r} - \mathbf{r}_1|. \tag{B1}$$

The $K_z(x)$ through the strip causes the potential

$$A_z^{(s)}(\mathbf{r}) \;=\; -\frac{\mu_0}{2\pi} \int_{-w}^{w} K_z(x') \ln|\mathbf{r} - \mathbf{r}'|\, dx', \tag{B2}$$

with $\mathbf{r}' = (x', 0)$ on the strip. The electric field is given by $E_z(\mathbf{r}) = -j\omega(A_z^{(1)}(\mathbf{r}) + A_z^{(s)}(\mathbf{r})) - \nabla_z V(\mathbf{r})$. The condition at the strip

$$E_z(x, 0) = K_z(x) R_\square \tag{B3}$$

results in a Fredholm integral equation of the second kind

$$K_z(x) - \lambda \int_{-w}^{w} K_z(x') \ln|x - x'|\, dx' = f(x) + c, \qquad -w \le x \le w, \tag{B4}$$

where $\lambda = j\omega\mu_0/2\pi R_\square$, $c = -\nabla_z V/R_\square$ and

$$f(x) = -j\omega A_z^{(1)}(x, 0)/R_\square \tag{B5}$$

the excitation function due to the wire. The width of the GP is here finite, in contrast to Appendix A. Consequently the current through the GP is smaller than $-I_1$ when $c = 0$. The constraint

$$\int_{-w}^{w} K_z(x)\, dx = -I_1 \tag{B6}$$

requires that some K_z should be added which is a solution of Eq. (B4) with $f(x) = 0$. For an isolated PCB, reciprocity of Z_t can be applied to show that $c = -Z_t(\text{1-CM}) I_1/R_\square$, in which Z_t(1-CM) is the transfer impedance between the DM circuit of wire 1 and GP on one hand and the CM circuit formed by the GP and a far away CP on the other hand. Because the reference position x^* on the GP in Eq. (16) is chosen arbitrarily, $E_z + j\omega(A_z^{(s)} + A_z^{(1)})$ is constant over the GP in the x-direction, as is $\nabla_z V$. When the difference of Eq. (B4) is taken for two positions x and x^* on the GP, c is eliminated.

The CM current distribution is a solution of Eqs. (B4) and (B6) with $f(x) = 0$. A comparison with Eq. (C8) shows that c is then equal to $-I_1\,[1/2w + (j\omega\mu_0/2\pi R_\square)\ln(2/w)]$

Similar to Eq. (A17) we can rewrite the Z_t in Eq. (1) to

$$Z_t = \left[j\omega A_z(x_s, y_s) - cR_\square\right]/I_1 \tag{B7}$$

where $A_z = A_z^{(s)} + A_z^{(1)}$ is the total vector potential taken at the sensing wire at (x_s, y_s).

Equation (B4) with constraint Eq. (B6) can also be solved analytically by expanding $K_z(x)$ and $f(x)$ in a series of Chebyshev polynomials [33]. The coefficients of the $f(x)$ are difficult

to obtain, and only closed form expressions have been found when the injection wire resides at the middle position of the strip. The off-diagonal elements in the resulting infinite matrix decrease slowly with the distance from the diagonal. The solution still requires numerical inversion and truncation of the matrix.

It is illustrative to show the connection between physics and the abstract mathematical theory of integral equations. Also, by means of the theory, it will be proved that the solution of Eq. (B4) is unique and continuous.[1] This last property is evident from a physical point of view, but mathematically less evident. The proof that a Fredholm equation of the second kind with continuous kernel possesses a continuous solution, is given in almost every standard text book on functional analysis or integral equations. For our weakly singular kernel we did not find the continuity proof in text books.

Let us introduce the Banach space $C[-w, w]$ consisting of continuous functions on $[-w, w]$ with maximum or infinite norm, i.e., for $g \in C[-w, w]$

$$\|g\|_\infty = \max_{t\in[-w,w]} |g(t)|.$$

The Hilbert space $L_2[-w, w]$ consists of Lebesgue measurable functions on $[-w, w]$ which are square integrable, that is, for $g \in L_2[-w, w]$

$$\int_{-w}^{w} |g(t)|^2 \, dt < \infty. \tag{B8}$$

Eq. (B4) can be written as

$$(\mathcal{I} - \lambda\mathcal{T})\, K_z \;=\; g, \tag{B9}$$

with $g \in C[-w, w]$, and the operator $\mathcal{T} : C[-w, w] \to C[-w, w]$ defined by

$$(\mathcal{T}K_z)(x) = \int_{-w}^{w} K_z(x') \ln|x - x'| \, dx'. \tag{B10}$$

It can be proved that $\mathcal{T}$ is compact on $C[-w, w]$; this proof will be given at the end of this appendix. The spectrum of $\mathcal{T}$ is denoted by $\sigma(\mathcal{T})$. Observe that the set $\sigma(\mathcal{T})\backslash\{0\}$ consists of countable (perhaps finite or even empty) eigenvalues only [34, 8.3-1]. By [34, 8.2-4] we can extend $\mathcal{T}$ to a continuous linear operator $\mathcal{T}_{ext} : L_2[-w, w] \to L_2[-w, w]$, defined by

$$(\mathcal{T}_{ext}K_z)(x) = \int_{-w}^{w} K_z(x') \ln|x - x'| \, dx'. \tag{B11}$$

Since the kernel $\ln|x - x'|$ is square integrable, $\mathcal{T}_{ext}$ is Hilbert-Schmidt and therefore compact on $L_2[-w, w]$, see e.g. Stakgold [35, pp. 352-3]. Since the kernel is symmetric, $\mathcal{T}_{ext}$ is self-adjoint on $L_2[-w, w]$. It can be proved that $\mathcal{T}_{ext}$ is a negative operator [36, Example 6.10]. Therefore we have a self-adjoint, negative, and compact operator on $L_2[-w, w]$. The spectrum $\sigma(\mathcal{T}_{ext})$ of $\mathcal{T}_{ext}$ is real, negative, and discrete. The spectral values, say $\lambda_j < 0$, are eigenvalues of the operator. Since $\mathcal{T}$ is compact and $\mathcal{T}_{ext}$ is a continuous extension of $\mathcal{T}$, the spectrum

[1]The authors are indebted to dr. ir. S. J. L. van Eijndhoven from the Department of Mathematics and Computing Science, for the useful suggestions made.

$\sigma(\mathcal{T}) \subseteq \sigma(\mathcal{T}_{ext})$. We conclude that the spectrum of $\mathcal{T}$ is real, negative, and discrete. Since λ is purely imaginary for our strip problem we have $\lambda \neq \lambda_j^{-1}$. According to the general theory, the homogeneous equation $g \equiv 0$ in Eq. (B9) has only the trivial solution $K_z \equiv 0$. In other words, there are no oscillations. This is physically understandable, because in our model we only have inductive energy, which is not related to capacitive energy. Any disturbance is damped by resistance. Since $(\mathcal{I} - \lambda\mathcal{T})$ is continuously invertible for all $\lambda(\neq \lambda_j^{-1})$, the inhomogeneous operator equation (B9) has a unique continuous solution. In operator theory this solution equals

$$K_z = (\mathcal{I} - \lambda\mathcal{T})^{-1} g. \tag{B12}$$

Our original integral equation (B4) has therefore one and only one continuous solution.

Finally we will prove that $\mathcal{T}$ is compact. Consider the more general case with operator $\widetilde{\mathcal{T}} : C[-w, w] \to C[-w, w]$, defined by

$$(\widetilde{\mathcal{T}} K_z)(x) = \int_{-w}^{w} K_z(x') \frac{h(x, x')}{|x - x'|^\alpha}\, dx', \quad h \in C([-w, w] \times [-w, w]), \quad 0 < \alpha < 1. \tag{B13}$$

Since

$$\ln|x - x'| = \frac{|x - x'|^\alpha \ln|x - x'|}{|x - x'|^\alpha}, \quad x \neq x',$$

compactness of $\widetilde{\mathcal{T}}$ implies compactness of $\mathcal{T}$.

Theorem 1 *Operator $\mathcal{T} : C[-w, w] \to C[-w, w]$ defined by Eq.* (B10) *is compact on $C[-w, w]$.*

Proof. Let B a subset of $C[-w, w]$, which is of course bounded. The operator $\widetilde{\mathcal{T}}$, and therefore $\mathcal{T}$, is compact when the image $\widetilde{\mathcal{T}}(B)$ is relatively compact, that is, when the closure $\overline{\widetilde{\mathcal{T}}(B)}$ is compact. For every $h \in C([-w, w] \times [-w, w])$ with $\|h(\cdot, \cdot)\|_\infty \leq M$ and for every $K_z \in B$, it follows that

$$\begin{aligned} \|\widetilde{\mathcal{T}} K_z\|_\infty &\leq \|K_z\|_\infty \max_{x \in [-w,w]} \int_{-w}^{w} \left| \frac{h(x, x')}{|x - x'|^\alpha} \right| dx' \leq M \|K_z\|_\infty \max_{x \in [-w,w]} \int_{-w}^{w} \frac{1}{|x - x'|^\alpha}\, dx' \\ &= M \|K_z\|_\infty \max_{x \in [-w,w]} \frac{1}{1 - \alpha} \left[(w + x)^{1-\alpha} + (w - x)^{1-\alpha} \right] = M \|K_z\|_\infty \frac{w^{1-\alpha}}{1 - \alpha}. \end{aligned}$$

Therefore the set $\widetilde{\mathcal{T}}(B)$ is bounded on $C[-w, w]$. Let us prove next that this set is equicontinuous, that is,

$$\forall_{\varepsilon > 0} \exists_{\delta > 0} \forall_{x_1, x_2 \in [-w,w]} \forall_{K_z \in B} : \left[|x_1 - x_2| < \delta \Longrightarrow |\widetilde{\mathcal{T}} K_z(x_1) - \widetilde{\mathcal{T}} K_z(x_2)| < \varepsilon \right].$$

Let $x_1, x_2 \in [-w, w]$, $x_1 < x_2$, and $K_z \in B$, then

$$\begin{aligned} |\widetilde{\mathcal{T}} K_z(x_2) - \widetilde{\mathcal{T}} K_z(x_1)| &= \left| \int_{-w}^{w} \left[\frac{h(x_2, x')}{|x_2 - x'|^\alpha} - \frac{h(x_1, x')}{|x_1 - x'|^\alpha} \right] K_z(x')\, dx' \right| \\ &\leq \|K_z\|_\infty \int_{-w}^{w} \left| \frac{h(x_2, x')}{|x_2 - x'|^\alpha} - \frac{h(x_1, x')}{|x_1 - x'|^\alpha} \right| dx' \end{aligned}$$

This last integral can be split into

$$\int_{-w}^{x_1} \cdots dx', \quad \int_{x_1}^{x_2} \cdots dx', \quad \int_{x_2}^{w} \cdots dx'.$$

An estimation of the first integral yields

$$\begin{aligned}
&\int_{-w}^{x_1} \left| \frac{h(x_2,x')}{(x_2-x')^\alpha} - \frac{h(x_1,x')}{(x_1-x')^\alpha} \right| dx' \\
\leq\ &\int_{-w}^{x_1} \left[\left| \frac{h(x_2,x')-h(x_1,x')}{(x_2-x')^\alpha} \right| + |h(x_1,x')| \left| \frac{1}{(x_2-x')^\alpha} - \frac{1}{(x_1-x')^\alpha} \right| \right] dx' \\
\leq\ &\frac{M_1}{1-\alpha} \left[(w+x_2)^{1-\alpha} - (x_2-x_1)^{1-\alpha} \right] + M_2 \int_{-w}^{x_1} \left[\frac{1}{(x_1-x')^\alpha} - \frac{1}{(x_2-x')^\alpha} \right] dx',
\end{aligned}$$

with

$$M_1 = \max_{x' \in [-w,w]} |h(x_2,x') - h(x_1,x')|, \quad M_2 = \max_{x' \in [-w,w]} |h(x_1,x')|. \tag{B14}$$

Since

$$\int_{-w}^{x_1} \left[\frac{1}{(x_1-x')^\alpha} - \frac{1}{(x_2-x')^\alpha} \right] dx' = \frac{1}{1-\alpha} \left[(w+x_1)^{1-\alpha} - (w+x_2)^{1-\alpha} + (x_2-x_1)^{1-\alpha} \right],$$

we conclude

$$\forall_{\varepsilon>0} \exists_{\delta>0} \forall_{x_1,x_2 \in [-w,w]} : \left[|x_1-x_2| < \delta \Longrightarrow \int_{-w}^{x_1} \left| \frac{h(x_2,x')}{|x_2-x'|^\alpha} - \frac{h(x_1,x')}{|x_1-x'|^\alpha} \right| dx' < \varepsilon \right].$$

The integral

$$\int_{x_2}^{w} \left| \frac{h(x_2,x')}{|x_2-x'|^\alpha} - \frac{h(x_1,x')}{|x_1-x'|^\alpha} \right| dx'$$

can be handled in a similar manner. Consider next

$$\begin{aligned}
&\int_{x_1}^{x_2} \left| \frac{h(x_2,x')}{(x_2-x')^\alpha} - \frac{h(x_1,x')}{(x'-x_1)^\alpha} \right| dx' \\
\leq\ &\int_{x_1}^{x_2} \left[\left| \frac{h(x_2,x')-h(x_1,x')}{(x_2-x')^\alpha} \right| + |h(x_1,x')| \left| \frac{1}{(x_2-x')^\alpha} - \frac{1}{(x'-x_1)^\alpha} \right| \right] dx' \\
\leq\ &\frac{M_1}{1-\alpha} (x_2-x_1)^{1-\alpha} + M_2 \int_{x_1}^{x_2} \left| \frac{1}{(x_2-x')^\alpha} - \frac{1}{(x'-x_1)^\alpha} \right| dx',
\end{aligned}$$

with M_1 and M_2 given by Eq. (B14). Further, the transformation $x' = (x_2-x_1)/(1+u)+x_1$ yields

$$\int_{x_1}^{x_2} \left| \frac{1}{(x_2-x')^\alpha} - \frac{1}{(x'-x_1)^\alpha} \right| dx' = 2(x_2-x_1)^{1-\alpha} \int_0^1 (1+u)^{\alpha-2} (u^{-\alpha}-1)\, du.$$

The integral $\int_0^1 (1+u)^{\alpha-2}(u^{-\alpha}-1)\,du$ is bounded, therefore

$$\forall_{\varepsilon>0}\exists_{\delta>0}\forall_{x_1,x_2\in[-w,w]}:\left[|x_1-x_2|<\delta\Longrightarrow\int_{x_1}^{x_2}\left|\frac{h(x_2,x')}{|x_2-x'|^\alpha}-\frac{h(x_1,x')}{|x_1-x'|^\alpha}\right|dx'<\varepsilon\right].$$

We conclude that $\widetilde{\mathcal{T}}(B)$ is equicontinuous. By Ascoli's theorem [34, 8.7-4] this set has a subsequence, say $(K_z^{(n)})$, which converges (in the norm on $C[-w,w]$). It follows that the closure $\overline{\widetilde{\mathcal{T}}(B)}$ is compact on $C[-w,w]$. □

Appendix C

1. Joukowski transform

Suppose the injection and sensing wire at coordinates z_1 resp. z_2 in the complex $z = x + jy$–plane (Fig. C1). The infinitely thin strip is located on the real axis $-w < x < w$. The wire at z_1 carries a current I_1, the strip a current $-I_1$. The Joukowski transform [37, pp. 58-60] and its inverse

$$\frac{z}{w} = \frac{1}{2}(t + \frac{1}{t}), \qquad t = \frac{z}{w} + \sqrt{\left(\frac{z}{w}\right)^2 - 1}, \tag{C1}$$

map the outside of the strip in the z-plane and the outside of a unit circle in the complex t-plane onto each other, see Fig. C1.

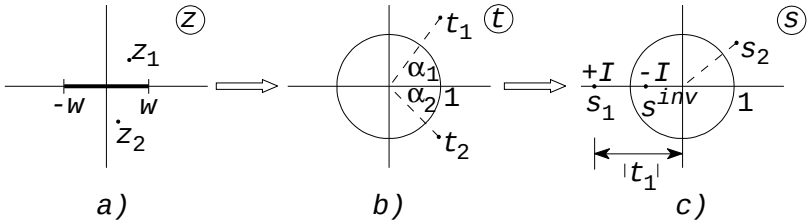

Fig. C1. The complex z, t and s-planes.

The square root in Eq. (C1) is to be understood as principal value

$$\sqrt{p^2 - 1} := \left|p^2 - 1\right|^{\frac{1}{2}} \mathrm{e}^{j(\arg(p-1)+\arg(p+1))/2}, \qquad -\pi < \arg(p \pm 1) \leq \pi. \tag{C2}$$

This definition avoids the use of Riemann surfaces, because the upper/lower side of the strip is mapped onto the upper/lower side of the circle by means of Eq. (C1). The transformation

$$s = te^{j(\pi - \alpha_1)}, \tag{C3}$$

rotates the transform t_1 (injection wire) onto the negative real axis of the $s = u + jv$–plane, with α_1 the principal value of the argument of t_1. The real part of the complex potential $\Omega(s) = X(s) + j\Psi(s)$ gives the magnetic field $\mathbf{H} = (\frac{\partial X}{\partial u}, \frac{\partial X}{\partial v})$. The imaginary part of the potential represents the flux function at position s. The unit circle must be a flux tube. The required complex potential is the sum of the potential due to the wire 1 at s_1 and of the potential due to a current $-I_1$ at the inverse point $s_1^{inv} = -|t_1|^{-1}$ of the injection wire (Fig. C1) [9]

$$\Omega(s) = -j\frac{I_1}{2\pi}\left[\log(s + |t_1|) - \log(s + \frac{1}{|t_1|})\right]. \tag{C4}$$

The principal value of the complex logarithm is used. The line dipole of strength $I(s_1 - s_1^{inv})$ is centered at $s = (s_1 + s_1^{inv})/2$. The mutual inductance M is equal to the difference in the flux function between the transform of z_2 and the unit circle

$$M = \frac{\Phi}{I_1} = \frac{\mu_0}{I_1}\left[\mathrm{Im}\ \Omega(s_2) - \mathrm{Im}\ \Omega(e^{j\phi_2})\right] = \frac{\mu_0}{I_1}\left[\Psi(s_2) - \Psi(e^{j\phi_2})\right], \tag{C5}$$

where $\phi_2 = \arg(s_2)$. The flux function on the circle is constant and is given by

$$\Psi(e^{j\phi_2}) = -\frac{I_1}{2\pi} \log |t_1|. \tag{C6}$$

Generally explicit real, closed forms for the mutual inductance cannot be calculated by means of Eqs. (C1), (C3), (C4), and (C5). Approximate analytical solutions for two limiting cases are given in the main text.

2. H-field lines for d.c.

A d.c. current I_1 is homogeneously distributed over the strip. The complex potential, used to plot the d.c. field in Fig. 4a, is obtained by integration of the logarithmic potential due to the strip:

$$\Omega(z) = -j\frac{I_1}{2\pi}\left[\log(z-z_1) + \frac{(z-z_3)\log(z-z_3) - (z-z_2)\log(z-z_2)}{z_3 - z_2} + 1\right], \tag{C7}$$

in which $z_{2,3}$ are the general endpoints of the strip. In our case $z_2 = -w$ and $z_3 = w$. When the injection wire at z_1 is close to the midpoint of the strip, the fieldlines assume the dipolar shape only at large distances $|z|$. The integral over the strip is identical to the expression given by Jaswon [21, Chapter 11].

3. CM current

For a high frequency common mode current I_{CM} through a GP with its return far away, the complex potential takes the form:

$$\Omega(t) = -j\frac{I_{CM}}{2\pi} \log t. \tag{C8}$$

At the GP holds $|t| = 1$ and thus $\Omega(\mathrm{e}^{j\phi}) = 0$. For M one obtains:

$$M = \frac{\Phi}{I_{CM}} = \frac{\mu_0}{I_{CM}} \mathrm{Im}\ \Omega(t_1) \tag{C9}$$

4. Parallel plates

Suppose we have the parallel plate system in the complex z–plane, see Fig. C2a. The width of the plates is $2w$ and their separation $2h_{CP}$. The transformation [10]

$$z = \frac{2K'h_{CP}}{\pi}\left[Z(s) + \frac{\pi s}{2KK'}\right], \tag{C10}$$

maps the upper side with cuts ABC and EFG of the z–plane onto the inner side of a rectangle in the complex $s = u + jv$–plane (Fig. C2b); K is the complete elliptic integral of the first kind of modulous k, K' the same integral with modulous $k' = \sqrt{1-k^2}$, and $Z(s)$ Jacobi's Zeta-function (see [19]). Note that Abramowitz [19] uses the parameter $m = k^2$ in the definition of the integrals. This derivation remains the same for both definitions.

If $h_{CP} \ll w$ the quotient of the integrals is given by [10, pp. 342]

$$\frac{K'}{K} = \frac{w}{h_{CP}}\left[1 + \frac{h_{CP}}{\pi w}\left(1 + \ln\frac{2\pi w}{h_{CP}}\right)\right]. \tag{C11}$$

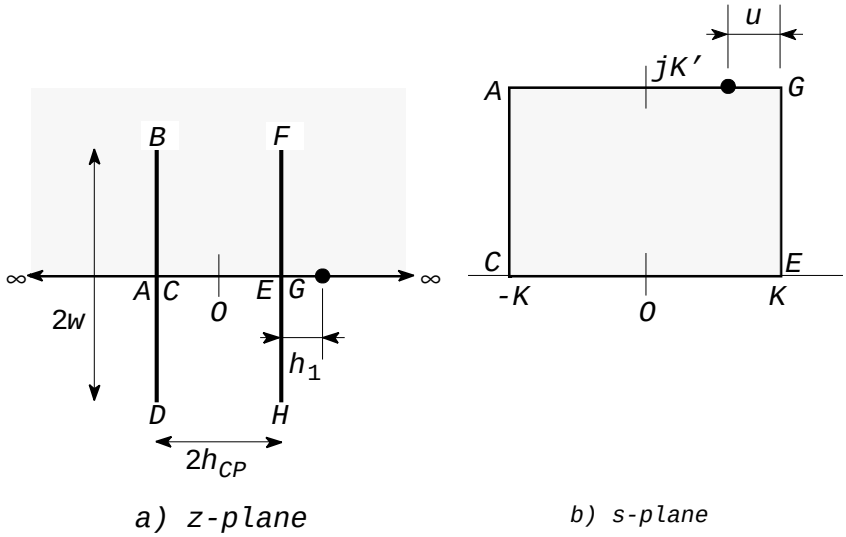

Fig. C2. The complex $z = x + jy$ and $s = u + jv$–planes for the parallel plates BD and FH.

Suppose now that the sensing wire resides near point G in the complex z–plane (Fig. C2a), say at $z = h_{CP} + h_1$, then its image resides at $s = K - u + jK'$. We assume that h_1 and u are small. When $K'/K \gg 1$, the q-series [19, Eq. (17.4.38)] of the Zeta-function yields

$$Z(s) = \frac{\pi}{K} \sum_{n=1}^{\infty} \frac{\sin \frac{n\pi s}{K}}{\sinh \frac{n\pi K'}{K}} \simeq \frac{2\pi}{K} \sum_{n=1}^{\infty} \mathrm{e}^{-n\pi \frac{K'}{K}} \sin \frac{n\pi s}{K} \tag{C12}$$

The sine-function in the summation simplifies for $s = K - u + jK'$ to

$$\sin \frac{n\pi s}{K} \approx \frac{j}{2} \mathrm{e}^{n\pi \frac{K'}{K}} \mathrm{e}^{-jn\pi \frac{K-u}{K}}, \tag{C13}$$

where the trigonometric sine-summation rule and $\sinh p \simeq \cosh p \simeq \mathrm{e}^p/2 \;\; (p = n\pi K'/K \gg 1)$ are used. Substitution of Eq. (C13) into Eq. (C12) yields

$$Z(K - u + jK') \simeq -\frac{j\pi}{2K} \left[1 + j \tan \frac{\pi u}{2K}\right]. \tag{C14}$$

Substitution of $z = h_{CP} + h_1$ and $s = K - u + jK'$ in Eq. (C10) finally results in the transcendental equation

$$h_{CP} + h_1 \simeq \frac{K'}{K} h_{CP} \left[\tan \frac{\pi u}{2K} + \frac{K - u}{K'}\right]. \tag{C15}$$

Because $K \simeq \pi/2$ and $u \ll 1$, the first order approximation of the tangent can be used $(\tan p \simeq p)$, and so

$$u \simeq \frac{2K^2}{h_{CP}(K'\pi - 2K)} h_1. \tag{C16}$$

The mutual inductance M then simply follows from

$$M = \mu_0 \frac{u}{2K'} \simeq \mu_0 \frac{K}{K'} \frac{1}{\frac{K'}{K}\pi - 2} \frac{h_1}{h_{CP}}. \tag{C17}$$

With $K'/K \simeq w/h_{CP} \gg 1$ one obtains the result presented in Sect. IV, Eq. (24).

5. Approximate solution

A simpler but approximate derivation for the problem of the previous subsection can be found when $h_{CP} \ll 2w$. The transform between $z = x + jy$ and $s = u + jv$

$$\frac{z}{z_0} = \mathrm{e}^{s/s_0} - \frac{s}{s_0} - 1 \tag{C18}$$

maps the strip $0 \leq v \leq \pi s_0$ in the s-plane on the z-plane with $y > -\pi z_0$; $s = 0$ is mapped onto $z = 0$ (Fig. C3). The origin of the coordinate system is now on the left edge of the GP. The image of the line $v = j\delta$ with $\delta \downarrow 0$ folds around the positive real axis in the z-plane.

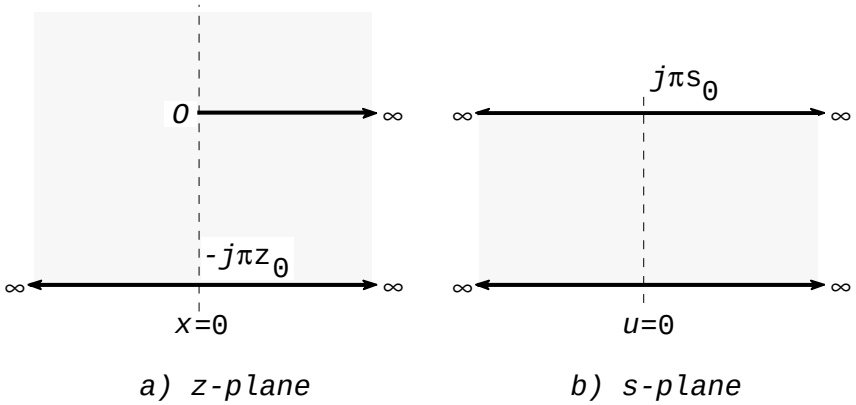

Fig. C3. The complex $z = x + jy$ and $s = u + jv$–plane for the fringing field effects of a parallel plate system.

In the s-plane we assume the parallel plate transmission line of infinite extent in the u-direction. A first approximation Φ_a of the flux per unit length between the plates is

$$\Phi_a = \mu_0 K_z h_{CP}, \tag{C19}$$

in which K_z is the sheet current density approximated by $I/2w$. The scaling factor s_0 for the flux function v in the s-plane is $\mu_0 K_z h_{CP}/\pi$; the scaling factor z_0 for the z-plane is then h_{CP}/π. When we expand the exponential in Eq. (C18) to the second degree, the first two terms cancel in the r.h.s. of Eq. (C18). For a point jy near the edge of the PCB $v/s_0 \simeq \sqrt{2|y|/z_0}$ holds approximately. The resulting M is presented as Eq. (25). Higher order terms in the expansion become soon important. In Fig. C4 we compare v from Eq. (C18) to the second order expansion with and without an additional correction term Δv fitted over the range $-1 < y/z_0 < 1$:

$$\Delta v/s_0 = \sum_{k=0}^{2} c_k \left(\frac{y}{z_0}\right)^k \quad \text{with} \quad \left\{ \begin{array}{lcl} c_0 & = & +0.0013 \\ c_1 & = & -0.3336 \\ c_2 & = & +0.0557 \end{array} \right. \tag{C20}$$

where y is positive above the GP. This second order fit is accurate to within 0.004 for v/s_0; if restricted to the linear term only to within 0.06. The markers on the abscissa correspond to the height of the sensing wire in Fig. 12.

For a point $z = w + jh_1$ above the middle line of the PCB, s is near the positive real axis; the exponent is the leading term in Eq. (C18). One may then approximate the flux function

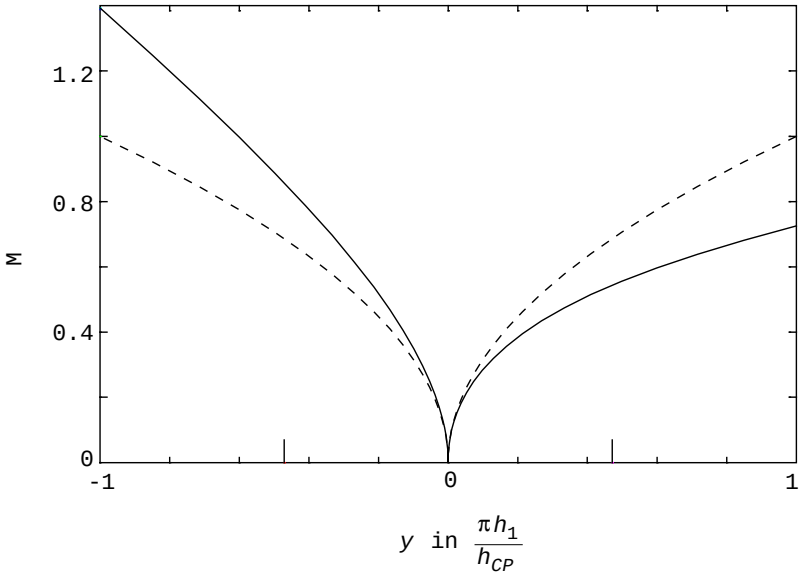

Fig. C4. The M-part of the CM to DM Z_t (—) in units $\mu_0 h_{CP}/2\pi w$, as function of height y of the sensing track at the edge of the GP. The approximation of Eq. (25) is also shown (- - -).

by

$$v \approx \text{Im } \log z = \arctan \frac{h_1}{w} \approx \frac{h_1}{w} \tag{C21}$$

The magnetic field lines between the GP and the CP forms closed loops around the GP. The other edge of the PCB is taken into account by assuming that both edges contribute independently. For the position $z = w + jh_1$ we multiply the above mentioned flux function by a factor 2. Application the scaling for s and z results in Eq. (24) given in the main text, which was also obtained at the end of the Appendix C4. For a point $z = w - jh_1$ under the middle line of the PCB, s is close to the negative real axis; the exponent in Eq. (C18) can be neglected. One easily verifies that the resulting M is equal Eq. (23) given in the main text.

In the comparison of the analytical values for M with the numerical and experimental values for sensing track positions close to the GP, the approximation of the total flux Φ in Eq. (C19) turned out to be too large even for small values of h_{CP}/w. Better approximations for Φ are given by Love [10, Sect. 3] and Kuester and Chang [25, Eq. (14)] which are repeated here for convenience:

$$\Phi \simeq \frac{\mu_0 I_{CM} h_{CP}}{2w} \left[1 + \frac{h_{CP}}{\pi w} \ln \frac{2\pi w}{h_{CP}}\right]^{-1} \quad \text{(Love)} \tag{C22}$$

$$\simeq \frac{\mu_0 I_{CM}}{2} \left[\frac{K[\text{sech}(\pi w/4h_{CP})]}{2K[\tanh(\pi w/4h_{CP})]} - \frac{h_{CP}^2}{2\pi w^2} \ln\left(1 + \frac{4w^2}{a h_{CP}^2}\right)\right] \quad \text{(K\&C)}, \tag{C23}$$

with $K(k)$ the complete elliptic integral and $a = 2/\ln(4/\pi)$. In Fig. C5 we compare Eq. (C19), (C22) and (C23); we used the last approximation for the M-curves in Fig. 12.

6. Track between two planes

In the $z = x + jy$-plane (Fig. C3) the origin is at the leftmost edge of the top plane; assume the other plane at $y = -2h_{PP}$ which also extends into the positive real direction. The plane

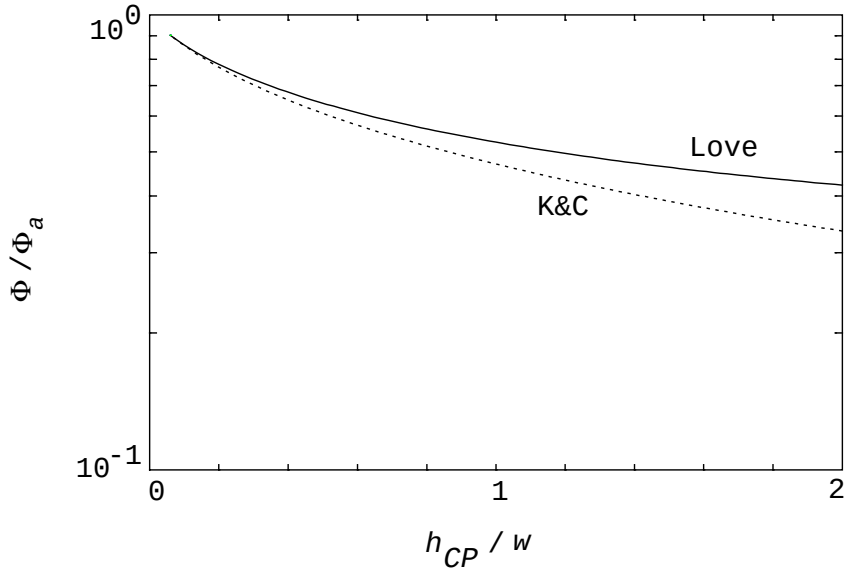

Fig. C5. The flux between a parallel plate system as derived by Love, Eq. (C22) and by Kuester and Chang (K&C), Eq. (C23) compared to the simple approximation of a homogeneous field, Eq. (C19).

$y = -jh_{PP}$ is a symmetry plane in which the injection wire 1 resides at $x_1 > 0$. Wire 1 carries a current I_1. The transformation Eq. (C18) and Fig. C3 can only be used for the region $y \geq -jh_{PP}$, which suffices in our case. The scaling factor in Eq. (C18) is $z_0 = h_{PP}/\pi$. Sensing wire 2 is at $z_2 = x_2 + jy_2$ above the top plane.

Assume now the injection wire 1 in the s-plane at the position $s_1 = u_1 + jv_1$ between two perfectly conducting planes at $v = \pm\pi$. The complex potential Ω which describes the H-field between the planes and which satisfies the boundary condition $\operatorname{Im}\Omega = 0$ at these planes is:

$$\Omega(s) = \frac{-j\mu_0 I_1}{2\pi} \log\left[\frac{\sinh[(s-s_1)/4]}{\cosh[(s-s_1^*)/4]}\right], \tag{C24}$$

with s_1^* the complex conjugate of s_1. If s_1 is midway between the planes, $v_1 = 0$ holds, and $\operatorname{Im}\Omega$ is symmetric w.r.t. the real axis.

For calculation of the mutual inductance, z_1/z_0 and z_2/z_0 are transformed by Eq. (C18) with $s_0 = 1$. Both s_1 and s_2 are shifted over $-j\pi$ before substitution in Eq. (C24). The resulting M is shown in Fig. 17. A further simplification is possible when wire 1 is deeply buried between the planes, i.e. $x_1 > h_{PP}$, and z_2 is above the top plane. Then $|s_2 - s_1|$ is large and the argument of the logarithm in Eq. (C24) is close to 1; the logarithm is then approximately $-2\,\mathrm{e}^{-(s_2-s_1)/2}$. The exponential in Eq. (C18) can be neglected in the transformation for z_1. With these approximations M becomes

$$M(x_1, z_2) = -\frac{\mu_0}{\pi}\operatorname{Im}\left[\sqrt{\frac{z_0}{z_2}}\mathrm{e}^{-(x_1+z_0)/2z_0}\right]. \tag{C25}$$

This may be further simplified to Eq. (33) for the sensing wire at larger distances from the edges; note that in the main text the z-coordinate system is shifted.

References

[1] Laan, P.C.T. van der and M.A. van Houten, A.P.J. van Deursen
Grounding philosophy.
In: Electromagnetic compatibility 1987. Proc. 7th International Zurich symposium and technical exhibition on electromagnetic compatibility. Zürich, 3-5 March 1987. Ed. by T. Dvořák. Zürich: ETH Zentrum, 1987. P. 567-572.

[2] Bergervoet, J.R.
EMC measurements and models connecting the system level with the module level.
Philips J. Res., Vol. 48 (1994), No's 1-2, p. 63-81.

[3] Gravelle, L.B. and P.F. Wilson
EMI/EMC in printed circuit boards: A literature review.
IEEE Trans. Electromagn. Compat., Vol. EMC-34 (1992), No. 2, p. 109-116.

[4] Djordjević, A.R. and T. K. Sarkar
Closed-form formulas for frequency-dependent resistance and inductance per unit length of microstrip and strip transmission lines.
IEEE Trans. Microwave Theory Tech., Vol. MTT-42 (1994), No. 2, p. 241-8.

[5] Cerri, G. and R. De Leo, V. Mariani Primiani, A. Schiavoni
Investigation of ground plane current distribution.
In: Electromagnetic compatibility 1993. Proc. 10th International Zurich symposium and technical exhibition on electromagnetic compatibility. Zürich, 9-11 March 1993. Zürich: ETH Zentrum, 1993. P. 195-200.

[6] Swainson, A.J.G.
Radiated emission, susceptibility and crosstalk control on ground plane printed circuit boards.
In: 7th Int. Conference on electromagnetic compatibility. York, 28-31 August 1990. London: IEE, 1990. P. 37-41.

[7] Ramo, S. and J.R. Whinnery, T. Van Duzer
Fields and waves in communication electronics. 3rd ed.
New York: Wiley, 1994.

[8] Laan, P.C.T. van der and W.J.L. Jansen, E.F. Steenis
Design of shielded enclosures, in particular for high-voltage laboratories.
Kema Sci. Tech. Rep., Vol. 2 (1984), No. 11, p. 101-111.

[9] Kaden, H.
Wirbelströme und Schirmung in der Nachrichtentechnik. 2nd ed.
Berlin: Springer, 1959.

[10] Love, A.E.H.
Some electrostatic distributions in two dimensions.
Proc. London Math. Soc., Ser. 2, Vol. 22 (1923), No. 1460, p. 337-369.

[11] Schelkunoff, S.A.
The electromagnetic theory of coaxial transmission lines and cylindrical sheets.
Bell Syst. Tech. J., Vol. 13 (1934), p. 532-579.

[12] Lipinski, W. and M. Gramz, P. Krason
Ein Beitrag zur Berechnung der Stromverdrängung in einem Bandleiter.
Arch. Elektrotech., Vol. 62 (1980), p. 51-55.

[13] Carson, J.R.
Wave propagation in overhead wires with ground return.
Bell Syst. Tech. J., Vol. 5 (1926), p. 539-554.

[14] Olsen, R.G.
Electromagnetic characteristics of horizontal and vertical wires above a dissipative earth.
Ph. D. thesis University of Colorado, 1974.

[15] Wedepohl L.M. and A.E. Efthymiadis
Wave propagation in transmission lines over lossy ground: A new complete field solution.
Proc. Inst. Electr. Eng., Vol. 125 (1978), No. 6, p. 505-510.

[16] Efthymiadis A.E. and L.M. Wedepohl
Propagation characteristics of infinitely-long single-conductor lines by the complete field solution method.
Proc. Inst. Electr. Eng., Vol. 125 (1978), No. 6, p. 511-517.

[17] Olyslager F. and D. De Zutter
High-frequency transmission line models for a thin wire above a conducting ground.
IEEE Trans. Electromagn. Compat., Vol. EMC-37 (1995), No. 2, p. 234-240, and references therein.

[18] Wise, W.H.
Effect of ground permeability on ground return conductors.
Bell Syst. Tech. J., Vol. 10 (1931), p. 472-484.

[19] Abramowitz M. and I.A. Stegun, Eds.
Handbook of mathematical functions. 9th printing.
New York: Dover, 1970.

[20] Harrington, R.F.
Field computations by moment methods.
New York: IEEE, 1993.

[21] Jaswon M.A. and G.T. Symm
Integral equation methods in potential theory and elastostatics.
London: Academic press, 1977.

[22] Helvoort, M.J.A.M. van
Grounding structures for the EMC-protection of cabling and wiring.
Ph.D. thesis Eindhoven University of Technology, 1995.

[23] Langton, N.H.
The parallel-plate capacitor with symmetrical placed unequal plates.
J. Electrost., Vol. 9 (1981), p. 289-305.

[24] Lin, W.
Computation of the parallel-plate capacitor with symmetrical placed unequal plates.
IEEE Trans. Microwave Theory Tech., Vol. MTT-33 (1985), No. 9, p. 800-807.

[25] Kuester E.F. and D. C. Chang
Closed-form expressions for the current or charge distribution on parallel strips or microstrips.
IEEE Trans. Microwave Theory Tech., Vol. MTT-28 (1980), No. 3, p. 254-259.

[26] Gradshteyn I.S. and I.M. Ryzhik
Table of integrals, series and products.
New York: Academic Press, 1967.

[27] Houten M.A. van and E.J.M. van Heesch, A.P.J. van Deursen, R.G. Noij, J.N.A.M. van Rooy, P.C.T. van der Laan
General methods for the protection of electronic equipment against interference, tested in high-voltage substations.
In: Electromagnetic compatibility 1989. Proc. 8th International Zurich symposium and technical exhibition on electromagnetic compatibility. Zürich, 7-9 March 1989. Ed. by T. Dvořák. Zürich: ETH Zentrum, 1989. P. 429-434.

[28] Helvoort, M.J.A.M. van and A.P.J. van Deursen, P.C.T. van der Laan
The transfer impedance of cables with a nearby return conductor and a noncentral inner conductor.
IEEE Trans. Electromagn. Compat., Vol. EMC-37 (1995), No. 2, p. 301-306.

[29] Ott, H.W.
Controlling EMI by printed wiring board layout.
In: Electromagnetic compatibility 1985. Proc. 6th International Zurich symposium and technical exhibition on electromagnetic compatibility. Zürich, 5-7 March 1985. Ed. by T. Dvořák. Zürich: ETH Zentrum, 1985. P. 127-132.

[30] Goedbloed, J.
Electromagnetic compatibility.
London: Prentice Hall, 1992.

[31] Bersier R. and B. Szentkuti
Rational and new experimental evidence on the adequacy of conducted instead of radiated susceptibility tests.
In: Electromagnetic compatibility 1983. Proc. 5th International Zurich symposium and technical exhibition on electromagnetic compatibility. Zürich, 8-10 March 1983. Ed. by T. Dvořák. Zürich: ETH Zentrum, 1983. P. 257-262.

[32] Bergervoet, J.R., private communication.

[33] Butler C.M. and D.R. Wilton
General analysis of narrow strip and slots.
IEEE Trans. Antennas Propagat., Vol. AP-28 (1980), No. 1, p. 42-48.

[34] Kreyszig, E.
Introductory functional analysis with applications.
New York: Wiley, 1978.

[35] Stakgold, I.
Green's functions and boundary value problems.
New York: Wiley, 1979.

[36] Porter D. and D.S.G. Stirling
Integral equations: A practical treatment, from spectral theory to applications.
New York: Cambridge University Press, 1990.

[37] Kober, H.
Dictionary of Conformal Representations. 2nd ed.
New York: Dover, 1957.